

# A mid-infrared spectroscopic atlas of local active galactic nuclei on sub-arcsecond resolution using GTC/CanariCam

A. Alonso-Herrero,<sup>1,2,3\*</sup> P. Esquej,<sup>4</sup> P. F. Roche,<sup>2</sup> C. Ramos Almeida,<sup>5,6†</sup> O. González-Martín,<sup>7</sup> C. Packham,<sup>3</sup> N. A. Levenson,<sup>8</sup> R. E. Mason,<sup>9</sup> A. Hernán-Caballero,<sup>1</sup> M. Pereira-Santaella,<sup>10,11</sup> C. Alvarez,<sup>5,6</sup> I. Aretxaga<sup>12</sup>, E. López-Rodríguez,<sup>3†</sup> L. Colina,<sup>10,11</sup> T. Díaz-Santos<sup>13</sup>, M. Imanishi,<sup>14,15,16</sup> J. M. Rodríguez Espinosa,<sup>5,6</sup> E. Perlman<sup>17</sup>

<sup>1</sup>Instituto de Física de Cantabria, CSIC-UC, E-39005 Santander, Spain

<sup>2</sup>Department of Physics, University of Oxford, Oxford OX1 3RH, UK

<sup>3</sup>Department of Physics and Astronomy, University of Texas at San Antonio, San Antonio, TX 78249, USA

<sup>4</sup>Departamento de Astrofísica, Universidad Complutense de Madrid, E-28040 Madrid, Spain

<sup>5</sup>Instituto de Astrofísica de Canarias (IAC), E-38205 La Laguna, Tenerife, Spain

<sup>6</sup>Departamento de Astrofísica, Universidad de la Laguna (ULL), E-38206 La Laguna, Tenerife, Spain

<sup>7</sup>Centro de Radioastronomía y Astrofísica (CRA-UNAM), 3-72 (Xangari), 8701, Morelia, Mexico

<sup>8</sup>Gemini Observatory, Casilla 603, La Serena, Chile

<sup>9</sup>Gemini Observatory, Northern Operations Center, Hilo, HI 96720, USA

<sup>10</sup>Centro de Astrobiología, CSIC-INTA, E-28850 Torrejón de Ardoz, Madrid, Spain

<sup>11</sup>ASTRO-UAM, Universidad Autónoma de Madrid, Unidad Asociada CSIC, Madrid, Spain

<sup>12</sup>Instituto Nacional de Astrofísica, Óptica y Electrónica (INAOE), 72000 Puebla, Mexico

<sup>13</sup>Núcleo de Astronomía de la Facultad de Ingeniería, Universidad Diego Portales, Av. Ejército Libertador 441, Santiago, Chile

<sup>14</sup>Subaru Telescope, 650 North A'ohoku Place, Hilo, Hawaii, 96720, USA

<sup>15</sup>National Astronomical Observatory of Japan, 2-21-1 Osawa, Mitaka, Tokyo 181-8588, Japan

<sup>16</sup>Department of Astronomical Science, The Graduate University for Advanced Studies (SOKENDAI), Mitaka, Tokyo 181-8588, Japan

<sup>17</sup>Florida Institute of Technology, Melbourne, FL 32901, USA

Accepted —. Received —; in original form —

## ABSTRACT

We present an atlas of mid-infrared (mid-IR)  $\sim 7.5 - 13 \mu\text{m}$  spectra of 45 local active galactic nuclei (AGN) obtained with CanariCam on the 10.4 m Gran Telescopio CANARIAS (GTC) as part of an ESO/GTC large program. The sample includes Seyferts and other low luminosity AGN (LLAGN) at a median distance of 35 Mpc and luminous AGN, namely PG quasars, (U)LIRGs, and radio galaxies (RG) at a median distance of 254 Mpc. To date, this is the largest mid-IR spectroscopic catalog of local AGN at sub-arcsecond resolution (median 0.3 arcsec). The goal of this work is to give an overview of the spectroscopic properties of the sample. The nuclear  $12 \mu\text{m}$  luminosities of the AGN span more than four orders of magnitude,  $\nu L_{12\mu\text{m}} \sim 3 \times 10^{41} - 10^{46} \text{ erg s}^{-1}$ . In a simple mid-IR spectral index vs. strength of the  $9.7 \mu\text{m}$  silicate feature diagram most LLAGN, Seyfert nuclei, PG quasars, and RGs lie in the region occupied by clumpy torus model tracks. However, the mid-IR spectra of some might include contributions from other mechanisms. Most (U)LIRG nuclei in our sample have deeper silicate features and flatter spectral indices than predicted by these models suggesting deeply embedded dust heating sources and/or contribution from star formation. The  $11.3 \mu\text{m}$  PAH feature is clearly detected in approximately half of the Seyfert nuclei, LLAGN, and (U)LIRGs. While the RG, PG quasars, and (U)LIRGs in our sample have similar nuclear  $\nu L_{12\mu\text{m}}$ , we do not detect nuclear PAH emission in the RGs and PG quasars.

**Key words:** galaxies: Seyfert – infrared: galaxies – galaxies: active – quasars: general

## 1 INTRODUCTION

The mid-infrared (mid-IR) range has been proven to be exceptionally rich in spectral features that can be used to characterise the properties of active galactic nuclei (AGN) and their host galaxies. In particular, *Spitzer* and previously ground-based and *ISO* spectroscopy have provided excellent mid-IR spectroscopy of large samples of local AGN (see e.g. Roche et al. 1991; Laurent et al. 2000; Buchanan et al. 2006; Tommasin et al. 2008; Wu et al. 2009; Tommasin et al. 2010). For instance, these observations allowed the study of the silicate dust near the AGN and in their host galaxies using the 10 and 18  $\mu\text{m}$  spectral features (Sturm et al. 2005; Shi et al. 2006; Thompson et al. 2009; Mor et al. 2009; Goulding et al. 2012) and define mid-IR features that trace star formation activity such as polycyclic aromatic hydrocarbon (PAH) features and the [Ne II]12.81  $\mu\text{m}$  line (Shi et al. 2007; Pereira-Santaella et al. 2010; Diamond-Stanic & Rieke 2012). Moreover, a number of different mid-IR indicators have been used to detect previously unidentified AGN in local galaxies (Goulding et al. 2009), look for buried AGN (Imanishi 2009; Alonso-Herrero et al. 2012) in local luminous and ultraluminous IR galaxies (LIRGs and ULIRGs, respectively), and provide a general activity class (Genzel et al. 1998; Spoon et al. 2007; Hernán-Caballero & Hatziminaoglou 2011).

While space-based mid-IR observations provide excellent sensitivity and access to large samples of AGN, ground-based mid-IR observations can take advantage of having telescopes with an order of magnitude larger diameters and therefore much higher angular resolution. Mid-IR instruments on 8-10 m telescopes deliver routinely imaging and spectroscopic observations with angular resolutions of typically 0.3-0.4 arcsec. This is approximately a factor of 10 better than what is achieved with *Spitzer*, albeit with limited sensitivity. So far, these high angular resolution mid-IR spectroscopic observations have been obtained for relatively small samples of AGN, although they are producing interesting results. These include the study of the properties of the AGN dusty torus (see e.g. Hönig et al. 2010; Alonso-Herrero et al. 2011; Ramos Almeida et al. 2014a; Ruschel-Dutra et al. 2014; Ichikawa et al. 2015), the star formation activity in the nuclear regions of local AGN (Sales et al. 2013; Esquej et al. 2014; Alonso-Herrero et al. 2014), the properties of the obscuring material in the nuclei of active galaxies (Mason et al. 2006; Roche et al. 2006, 2007; González-Martín et al. 2013; Roche et al. 2015), the nature of the nuclear dust heating source in local (U)LIRGs (Soifer et al. 2002; Lira et al. 2008; Díaz-Santos et al. 2010; Alonso-Herrero et al. 2013; Mori et al. 2014; Martínez-Paredes et al. 2015; Pereira-Santaella et al. 2015), and obscured super star clusters (Snijders et al. 2006).

In this paper we present a mid-IR spectroscopic atlas of 45 local AGN with accompanying imaging obtained with the CanariCam instrument (Telesco et al. 2003; Packham et al. 2005) on the 10.4 m Gran Telescopio CANARIAS (GTC) in El Roque de los Muchachos Observatory. The nearly diffraction limited (median 0.3 arcsec) imaging and spectroscopic observations were taken as part of an ESO/GTC large pro-

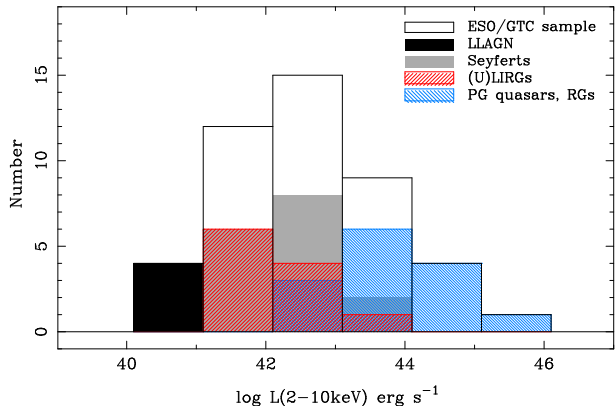


**Figure 1.** Hard X-ray luminosities of the AGN in the ESO/GTC sample. The filled and hatched histograms represent different AGN classes in the sample.

gram (ID 182.B-2005, PI Alonso-Herrero). The main goal of this work is to provide a brief overview of the mid-IR spectroscopic properties of the nuclear regions of local AGN. The paper is organized as follows. In Section 2 we present the main goals of our mid-IR survey of local AGN and the sample. Section 3 describes the data reduction and analysis of the mid-IR spectroscopic observations and accompanying mid-IR imaging observations. In Section 4 we discuss the main spectroscopic properties of the AGN sample and Section 5 summarizes our results.

## 2 THE GTC/CANARICAM MID-IR SURVEY OF LOCAL AGN

The main objective of our CanariCam mid-IR survey of local AGN is to understand the properties of the obscuring material around active nuclei, including the so-called torus of the AGN Unified Model (Antonucci 1993; Netzer 2015). In particular this survey was designed to address a number of open questions such as, (1) the nature of the torus material and its connection with the interstellar material in the host galaxy, (2) the dependence of the torus properties (e.g., torus physical and angular size, number of clouds, covering factor) on the AGN luminosity and/or activity class, (3) the relation between the dust properties (for instance, composition, grain size) and the AGN luminosity/type, and (4) the role of nuclear (< 100 pc) starbursts in feeding and/or obscuring the active nuclei of galaxies.

Although our team and others have already addressed some of the open questions posed above, this was done for relatively small samples of local AGN (see references in the Introduction). We thus decided to exploit the unique combination of the diffraction limited ( $\simeq 0.3$  arcsec) angular resolution and the imaging and spectroscopy capabilities of the GTC/CanariCam system to address these questions. We were awarded total of 180 hours of observing time through an ESO/GTC large program (see Section 3 for full details of these observations). In future papers we will combine the ESO/GTC time with the on-going (at the time of writing this paper) observations of  $\sim 100$  hours of CanariCam guaranteed time (GT) devoted to AGN science observations. The

‡ Research Affiliate-Postdoctoral, Department of Astronomy, University of Texas at Austin

**Table 1.** The ESO/GTC large program sample of local AGN

Name	Redshift	Dist (Mpc)	scale (kpc/arcsec)	Type	IRAS12 $\mu\text{m}$ (Jy)	Ref	Other Name
3C273	0.158339	734.	2.647	RG/PG Quasar	0.417	1	PG 1226+023
3C382	0.05787	246.	1.068	RG	0.071	2	
3C390.3	0.056100	239.	1.041	RG	0.140	2	
IRAS 08572+3915	0.058350	254.	1.097	(U)LIRG/Sy2:(NW)/Sy2:(SE)	0.33	3	
IRAS 13197-1627	0.016541	73.2	0.343	(U)LIRG/Sy1.8	0.94	3	MCG-03-34-064
IRAS 13349+2438	0.107641	483.	1.905	(U)LIRG/Sy1	0.631	4	
IRAS 14348-1447	0.08300	366.	1.512	(U)LIRG/ cp:(NE)/cp:(SW)	<0.10	3	
IRAS 17208-0014	0.042810	181.	0.809	(U)LIRG/HII	0.22	3	
Mrk 3	0.013509	55.9	0.264	Sy2	0.760	4	
Mrk 231	0.042170	181.	0.807	(U)LIRG/Sy1	1.83	3	IRAS 12540+5708
Mrk 463	0.050355	219.	0.959	(U)LIRG/Sy2(E)	0.510	4	IRAS 13536+1836
Mrk 478	0.079055	347.	1.443	PG Quasar	0.098	1	PG 1440+356
Mrk 841	0.036422	157.	0.706	PG Quasar	0.109	1	PG 1501+106
Mrk 1014	0.163110	748	2.684	PG Quasar/(U)LIRG	0.137	1	PG 0157+002
Mrk 1066	0.012025	47.2	0.224	Sy2	0.460	3	UGC 02456
Mrk 1073	0.023343	95.3	0.442	(U)LIRG/Sy2	0.440	3	UGC 02608
Mrk 1210	0.013496	59.5	0.280	Sy2	0.496	4	
Mrk 1383	0.086570	383.	1.571	PG Quasar	0.124	1	PG 1426+015
NGC 931	0.016652	66.1	0.310	Sy1	0.610	4	Mrk 1040
NGC 1194	0.013596	53.7	0.254	Sy1.9	0.266	4	
NGC 1275	0.017559	70.9	0.332	RG/Sy1.5	1.06	3	3C84
NGC 1320	0.008883	34.5	0.164	Sy2	1.069	4	
NGC 1614	0.015938	65.5	0.308	(U)LIRG/cp	1.38	3	IRAS 04315-0840
NGC 2273	0.006138	25.8	0.124	Sy2	0.44	3	
NGC 2992	0.007710	36.6	0.174	Sy1.8	0.63	3	
NGC 3227	0.003859	20.4	0.098	Sy1.5	0.94	3	
NGC 4051	0.002336	12.7	0.061	Sy1	1.35	3	
NGC 4253	0.01292	57.6	0.272	Sy1	0.386	4	
NGC 4258	0.001494	8.97	0.043	LLAGN/Sy1.9	2.25	5	M106
NGC 4388	0.008419	17.0*	0.082	Sy1.9	0.29	3	
NGC 4419	0.000871	17.0*	0.082	LLAGN/T2	0.67	3	
NGC 4569	-0.000784	17.0*	0.082	LLAGN/T2	1.27	3	M90
NGC 4579	0.005060	17.0*	0.082	LLAGN/Sy1.9	1.12	3	M58
NGC 5347	0.007789	35.1	0.167	Sy2	0.309	4	
NGC 5548	0.017175	74.5	0.348	Sy1.5	0.401	4	
NGC 5793	0.011645	51.1	0.242	Sy2	0.17	3	
NGC 6240	0.024480	103.	0.475	(U)LIRG/LINER	0.59	3	IRAS 16504+0228
NGC 7465	0.006538	21.9	0.105	Sy2	0.26	3	
OQ208	0.076576	336.	1.406	RG	<0.185	4	Mrk 668
PG 0804+761	0.100000	443.	1.773	PG Quasar	0.190	1	
PG 0844+349	0.064000	279.	1.194	PG Quasar	0.126	1	
PG 1211+143	0.080900	358.	1.484	PG Quasar	0.362	1	
PG 1229+204	0.063010	276.	1.183	PG Quasar	0.417	1	
PG 1411+442	0.089600	396.	1.615	PG Quasar	0.115	1	
UGC 5101	0.039367	168.	0.755	(U)LIRG/Sy2:	0.25	3	IRAS 09320+6134

*Notes.* Redshifts, luminosity distances, and projected 1 arcsec scales are from NED for  $H_0 = 73 \text{ km s}^{-1} \text{ Mpc}^{-1}$ ,  $\Omega_M = 0.27$ , and  $\Omega_\Lambda = 0.73$ . \*These galaxies are in the Virgo Cluster (Binggeli et al. 1985). In the column of "Type", the single colons mean that the nucleus does not have the same classification in the three optical diagrams used and double colons mean that the classification using different optical line ratios does not agree on any of the diagrams (see Yuan et al. 2010 for details). If two optical classes are given, they refer to the individual nuclei of the system. The *IRAS* 12  $\mu\text{m}$  flux densities are taken from the reference listed in the column to the right. References. 1. Sanders et al. (1989). 2. Golombek et al. (1988). 3. *IRAS* Revised Bright Galaxy Sample (RBGS), Sanders et al. (2003). 4. *IRAS* Faint Catalog (IRASFC), Moshir et al. (1990). 5. Rice et al. (1988).

final goal is to build a statistically significant sample of local AGN in terms of AGN classes and AGN luminosity bins (see below). As part of the ESO/GTC and GT observations we are also obtaining mid-IR imaging and spectropolarimetry observations of some of the brightest targets in our sample (López-Rodríguez et al. 2014, 2015, López-Rodríguez et al. 2016, in preparation).

For the ESO/GTC large program we selected a sam-

ple of 45 local active galaxies with the purpose of covering a broad range of AGN luminosities and different AGN classes. We chose the hard (2-10 keV) X-ray luminosities as a proxy for the AGN luminosity. Finally, to ensure a spectroscopic detection with reasonable integration times we also imposed sufficiently bright arcsecond resolution literature *N*-band fluxes. This limit was approximately 20 mJy. The ESO/GTC sample of local AGN (see Table 1) includes transition (T)

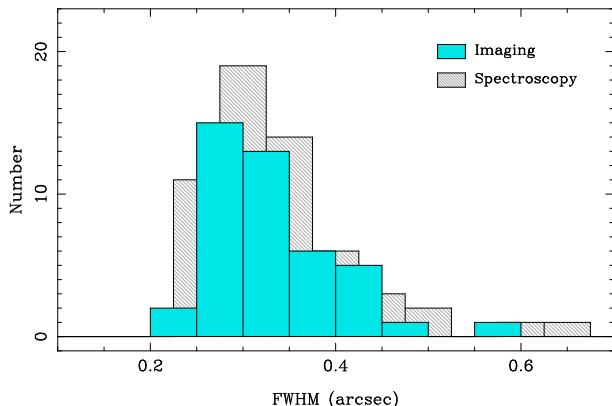


**Figure 2.** Image quality of the GTC/CanariCam imaging and spectroscopic observations in the ESO/GTC large program as measured from the FWHM of the standard stars at  $8.7\ \mu\text{m}$ .

or composite (cp) objects (that is, nuclei with contributions from AGN and star formation activity), Seyfert galaxies, radio galaxies (RG), LIRGs and ULIRGs, and quasars from the Bright Quasar Survey (Schmidt & Green 1983), which are selected from the Palomar-Green (PG) Survey. All galaxies in the (U)LIRG class, except IRAS 17208-0014, have been spectroscopically identified as AGN or composite (see Wu et al. 2009; Yuan et al. 2010). For those (U)LIRGs with double nuclei (see Section 3.1) at least one nucleus is spectroscopically classified as an AGN, usually the mid-IR bright one. The ULIRG sample was chosen to match approximately the PG quasars in AGN bolometric luminosities (see also Section 4.1).

It has been suggested that the torus disappears at AGN bolometric luminosities  $< 10^{42}\ \text{erg s}^{-1}$  (Elitzur & Shlosman 2006). To draw particular attention to AGN below this possible threshold, we identify objects with hard X-ray luminosities  $< 10^{41}\ \text{erg s}^{-1}$  as low-luminosity AGN (LLAGN). In summary, our sample contains 4 LLAGN, 16 Seyfert nuclei, 11 (U)LIRG, 5 RGs, and 9 PG quasars. We note that some (U)LIRG nuclei, and RG galaxies are also classified optically as Seyferts.

Fig. 1 shows the distribution of hard X-ray luminosities of the AGN in the ESO/GTC sample. As can be seen from this figure, the AGN luminosities span more than four orders of magnitude with the PG quasars and RGs at the high luminosity end. For the assumed cosmology ( $H_0 = 73\ \text{km s}^{-1}\ \text{Mpc}^{-1}$ ,  $\Omega_M = 0.27$ , and  $\Omega_\Lambda = 0.73$ ), the Seyferts and LLAGN are at a median distance of 35 Mpc, whereas the rest of the sample is at a median distance of 254 Mpc. The requirement that the nuclei for the galaxies in our sample be classified as AGN or composite using optical spectroscopy might exclude highly obscured AGN. We also note that the small-aperture mid-IR flux limit provides a mid-IR flux limited AGN sample, although some of the ULIRG nuclei and LLAGN also have a significant star formation contribution in the mid-IR (see e.g., Mason et al. 2012; Mori et al. 2014; Martínez-Paredes et al. 2015, and Alonso-Herrero et al. 2016, in preparation).

### 3 OBSERVATIONS, DATA REDUCTION, AND ANALYSIS

In this section we describe the CanariCam imaging and spectroscopic observations taken within the ESO/GTC large program as well as the data reduction and analysis. The ESO/GTC CanariCam imaging and spectroscopic observations were obtained between March 2012 and March 2015. As required by our approved ESO/GTC large program, all the data were observed in queue mode under photometric conditions and image quality better than 0.6 arcsec measured at mid-IR wavelengths from the full width half maximum (FWHM) of the standard stars (see Sections 3.1 and 3.2).

#### 3.1 Imaging observations and data reduction

We obtained imaging observations using the Si-2 filter, which has a central wavelength of  $\lambda_c = 8.7\ \mu\text{m}$  and a width at 50% cut-on/off of  $\Delta\lambda_{\text{cut}} = 1.1\ \mu\text{m}$ . We chose the Si-2 filter because it gives the optimal sensitivity with the best FWHM among the CanariCam filters. We observed all AGN in our sample except for two LLAGN (NGC 4258 and NGC 4579) and the LIRG NGC 1614<sup>1</sup>, which had been previously observed by Mason et al. (2012) and Díaz-Santos et al. (2008), respectively. The plate scale of the CanariCam  $320 \times 240$  Si:As detector is  $0.0798\ \text{arcsec pixel}^{-1}$  ( $0.08\ \text{arcsec pixel}^{-1}$  hereafter), which provides a field of view in imaging mode of  $26\ \text{arcsec} \times 19\ \text{arcsec}$ .

All the observations were carried out in observing blocks (OB) using the standard mid-IR chop-nod technique. The typical imaging sequence included an OB for the galaxy target with one or several repetitions together with an OB for the standard star, which was observed immediately before or after the galaxy observation. We used the observations of the standard stars to both perform the photometric calibration of the galaxy images and measure the angular resolution of the observations. The chop and nod throws were 15 arcsec, whereas the chop and nod angles, which were the same for the galaxy and the star, were chosen for each target to avoid extended galaxy emission in the sky images.

Table 2 summarizes the details of the imaging observations including the date of the observation, the on-source integration time, number of repetitions, position angle (PA) of the detector on the sky, and the name of the standard star. Observations taken prior to March 2013 were obtained with the S1R1-CR readout mode which greatly reduced the vertical "level drop" pattern (Sako et al. 2003) although it also produced a pattern noise resembling horizontal stripes in the images<sup>2</sup>. After March 2013 all the observations were taken with the S1R3 mode which is now the default mode for CanariCam<sup>3</sup>. This level drop effect did not affect our Ca-

<sup>1</sup> We note that we used the NGC 1614 acquisition image for the CanariCam spectroscopy (see next section) for the aperture photometry in Section 3.3.

<sup>2</sup> The horizontal stripes are clearly seen in the commissioning images of the CanariCam polarimetric mode: [http://www.gtc.iac.es/instruments/canaricam/data-commissioning.php#Pol\\_readout\\_mode](http://www.gtc.iac.es/instruments/canaricam/data-commissioning.php#Pol_readout_mode)

<sup>3</sup> We refer the reader to the GTC/CanariCam webpage for further information on the different readout modes:

**Table 2.** Log of the GTC/CanariCam Si-2 filter imaging observations.

Galaxy	Date (yyyy-mm-dd)	$t_{\text{on}} \times \text{rep}$ (s)	PA (degree)	Star	FWHM (arcsec)	Comment
3C273	2014-03-17	139 × 3	0	HD 107328	0.31	
3C382	2013-08-27	348 × 3	0	HD 176670	0.23	
3C390.3	2013-07-22	348 × 3	0	HD 158986	0.29	
IRAS 08572+3915	2014-03-16	139 × 3	0	HD 83787	0.28	
IRAS 13197–1627	2013-01-07	81 × 4	0	HD 116870	0.25	Pattern Noise
IRAS 13349+2438	2013-07-22	139 × 3	0	HD 121710	0.31	
IRAS 14348–1447	2014-06-10	348 × 3	0	HD 130157	0.40	
IRAS 17208–0014	2013-06-07	348 × 3	0	HD 157999	0.27	
Mrk 3	2013-08-27	139 × 3	0	HD 34450	0.49	
Mrk 231	2013-01-07	81 × 4	0	HD 111335	0.34	Pattern Noise
Mrk 463	2014-02-09	139 × 1	0	HD 125560	0.37	Distorted PSF
Mrk 478	2014-03-16	209 × 3	0	HD 128902	0.25	
Mrk 841	2013-08-30	209 × 4	0	HD 140573	0.26	
Mrk 1014	2013-01-01	242 × 3	0	HD 10550	0.59	Pattern Noise
Mrk 1066	2013-08-27	139 × 3	45	HD 18449	0.24	References 1, 2
Mrk 1073	2013-08-27	209 × 3	345	HD 19476	0.26	Reference 1
Mrk 1210	2012-12-28	147 × 3	0	HD 66141	0.31	Pattern Noise
Mrk 1383	2012-03-09	220 × 3	0	HD 126927	0.42	Pattern Noise
NGC 931	2013-08-26	139 × 3	350	HD 14146	0.28	
NGC 1194	2013-08-28	209 × 3	40	HD 20356	0.32	
NGC 1275	2013-08-27	139 × 4	0	HD 19476	0.37	
NGC 1320	2013-01-03	161 × 3	0	HD 20356	0.30	Distorted PSF
NGC 1614	2013-09-18	139 × 1	0	HD 28749	0.35	Acquisition image
NGC 2273	2013-09-24	209 × 3	20	HD 42633	0.26	Reference 1
NGC 2992	2014-02-13	348 × 2	30	HD 82660	0.32	Distorted PSF
NGC 3227	2014-03-17	209 × 3	55	HD 85503	0.31	
NGC 4051	2014-02-09	139 × 3	40	HD 95212	0.32	Distorted PSF
NGC 4253	2014-03-17	139 × 3	15	HD 108381	0.32	
NGC 4388	2015-02-01	348 × 3	90	HD 111067	0.39	
NGC 4419	2014-05-23	209 × 3	40	HD 109511	0.33	
NGC 4569	2014-03-16	209 × 3	300	HD 111067	0.28	
NGC 5347	2014-03-16	139 × 3	15	HD 121710	0.27	
NGC 5548	2014-03-17	139 × 3	0	HD 127093	0.44	
NGC 5793	2014-05-17	209 × 3	45	HD 133774	0.30	
NGC 6240	2013-08-27	209 × 3	286	HD 151217	0.38	References 1, 3
NGC 7465	2013-08-27	348 × 3	60	HD 220363	0.38	Distorted PSF
OQ208	2014-03-17	209 × 3	0	HD 127093	0.43	
PG 0804+761	2014-01-03	209 × 3	0	HD 64307	0.34	Distorted PSF
PG 0844+349	2014-01-06	216 × 2	0	HD 81146	0.38	Distorted PSF
PG 1211+143	2014-03-14	209 × 3	0	HD 107328	0.29	
PG 1229+204	2014-06-08	1251 × 1	0	HD 111067	0.27	
PG 1411+442	2014-03-16	209 × 3	0	HD 128902	0.27	
UGC 5101	2014-01-06	1224 × 1	0	HD 79354	0.41	Reference 4

*Notes.* The references listed in the last column indicate previous works where the galaxies have been presented. 1. Alonso-Herrero et al. (2014). 2. Ramos Almeida et al. (2014b). 3. Mori et al. (2014). 4. Martínez-Paredes et al. (2015).

nariCam science observations and the new readout model resulted in a signal-to-noise gain. The observations taken with the SIR1-CR readout mode are marked in the last column of Table 2.

We reduced the CanariCam imaging data using the REDCAN pipeline (see González-Martín et al. 2013). The reduction process of the imaging data includes sky subtraction, stacking of the individual images, and rejection of bad images. The flux calibration of the galaxy images is done using the observation of the standard star taken immediately before or after the galaxy OB. In those cases with several

repetitions for the same galaxy, we shifted the individual images to a common position and then combined them using the average. We finally rotated them to the usual orientation of north up, east to the left.

To estimate the angular resolution of the imaging observations we measured the FWHM of the standard star using a moffat function. These are listed in Table 2 and plotted in Fig. 2. As can be seen from this figure, the measured FWHM of the imaging observations are between 0.23 and 0.59 arcsec with a median value of 0.31 arcsec. At the median distances of our sample, this corresponds to a median physical resolution of approximately 51 pc for the Seyfert galaxies and LLAGN and 382 pc for the rest of the sample.

Apart from the FWHM, we also measured the Strehl

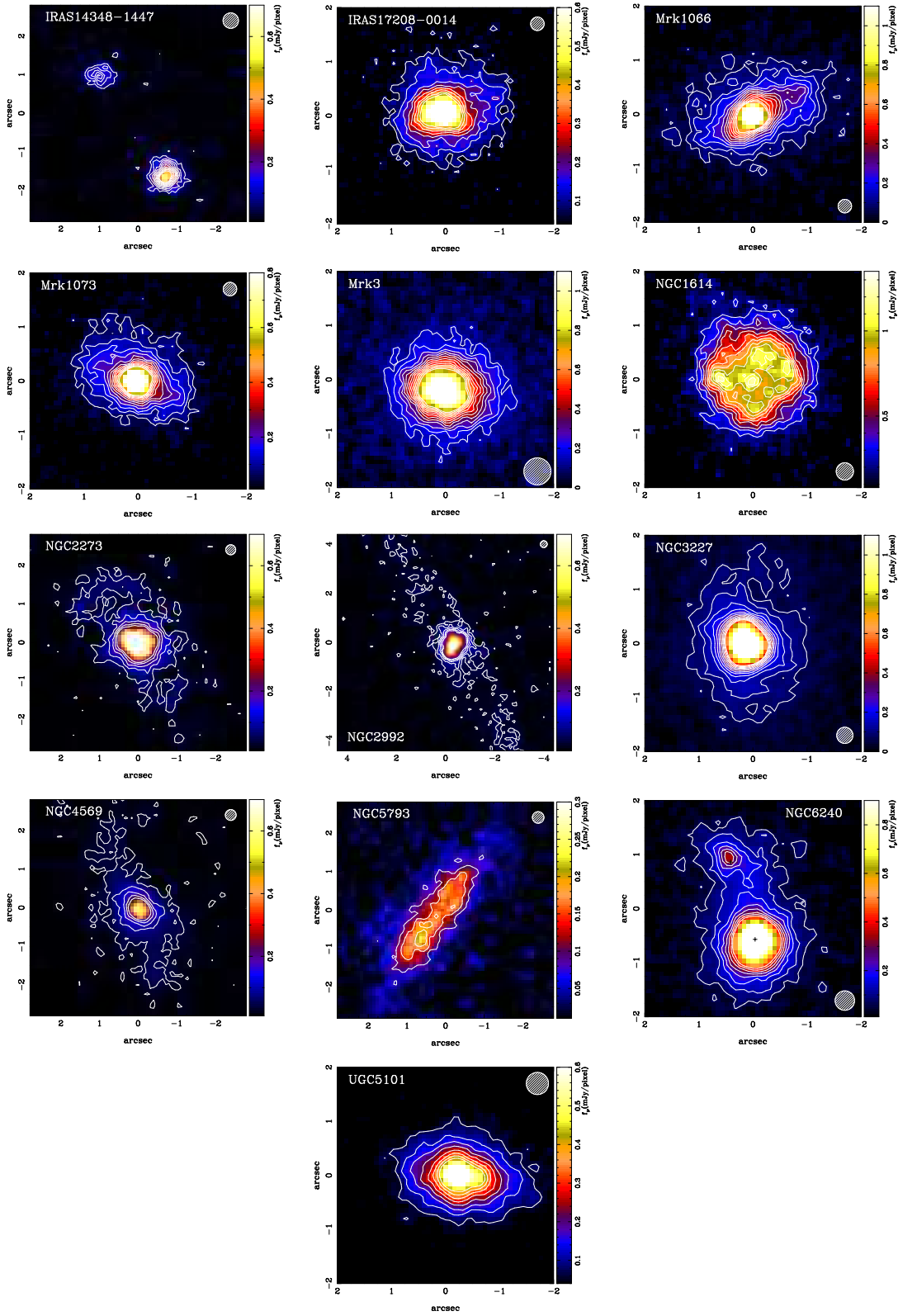


**Figure 3.** Examples of flux-calibrated GTC/CanariCam Si-2 ( $\lambda_c = 8.7 \mu\text{m}$ ) images of galaxies in the ESO/GTC large program which are clearly extended in the mid-IR. Orientation is north up, east to the left. We smoothed the CanariCam images with a Gaussian function with a width (sigma) between 0.6 and 0.7 pixels. The hatched circle represents the angular resolution of the image (FWHM) as measured from the corresponding standard star of each galaxy.

ratios of the standard stars. The median value for the imaging observations was 0.19, although we note that at the time the observations the GTC did not have fast tip/tilt guiding. A small fraction of the images show distorted shapes for the core of the point spread function (PSF). These images have lower Strehl ratios than expected for the measured FWHM of the star. For reference we marked those in the last column of Table 2.

Four (U)LIRGs in our sample have double nuclei, namely, IRAS 08572+3915, IRAS 14348–1447, Mrk 463 (see e.g., García-Marín et al. 2009), and NGC 6240. The CanariCam 8.7  $\mu\text{m}$  image of IRAS 08572+3915 only shows emission from one bright nucleus (see also Soifer et al. 2000). A comparison with archival *Spitzer*/IRAC images of this system at 3.4  $\mu\text{m}$  and 8  $\mu\text{m}$  reveals that the bright source detected in the mid-IR corresponds to the nucleus of the northern galaxy, which appears unresolved (FWHM=0.3 arcsec  $\approx$  330 pc) in our CanariCam 8.7  $\mu\text{m}$  image. The CanariCam image of IRAS 14348–1447 (see Fig. 3) reveals 8.7  $\mu\text{m}$  emission arising from both nuclei, with the southern one being brighter than the northern one (see Section 3.3 and Table 4). The CanariCam 8.7  $\mu\text{m}$  imaging data of NGC 6240 has been extensively discussed by Mori et al. (2014) and Alonso-Herrero et al. (2014). Soifer et al. (2002) obtained Keck mid-IR imaging and spectroscopy of Mrk 463 and showed that the emission comes from the eastern nucleus.

A large fraction of the AGN observed in the ESO/GTC large program show compact emission in the mid-IR, as already found in the large mid-IR imaging compilation of Asmus et al. (2014). In Fig. 3 we show the CanariCam images of those AGN in our sample that are clearly extended in the mid-IR. For completeness we also show galaxies already studied in some of our previous work (Alonso-Herrero et al. 2014; Ramos Almeida et al. 2014b; Mori et al. 2014; García-Bernete et al. 2015; Martínez-Paredes et al. 2015, see also Table 2). In a series of forthcoming papers we will present detailed analyses of the mid-IR nuclear and extended emission of Seyfert galaxies (García-Bernete et al. 2016 in preparation) and of PG quasars (Martínez-Paredes et al. 2016 in preparation).

### 3.2 Spectroscopic observations and data reduction

We used the CanariCam low spectral resolution ( $R = \lambda/\Delta\lambda \sim 175$ )  $N$ -band grating to obtain  $\sim 7.5 - 13 \mu\text{m}$  spectroscopy of the nuclear regions of 45 local AGN using the 0.52 arcsec wide slit. As for the imaging data, all the spectroscopic observations were taken using separate OBs for the galaxy and the standard star. Within a spectroscopy OB the observing sequence was to rotate the detector to the requested PA of the slit, take an acquisition image of the target (either galaxy or star) using the Si-2 filter, then place the slit, and finally integrate for the requested on-source time and number of repetitions. We chose the PA of the slit based on the extension of the mid-IR emission if that information existed or otherwise along the major axis of the galaxy. The chop-nod parameters were the same as for the imaging observations. The OB of the corresponding standard star was executed right before or after the galaxy OB. We used the observations of the standard stars to derive the photometric calibration, the telluric correction, the slit loss correction, and the FWHM of the observations.

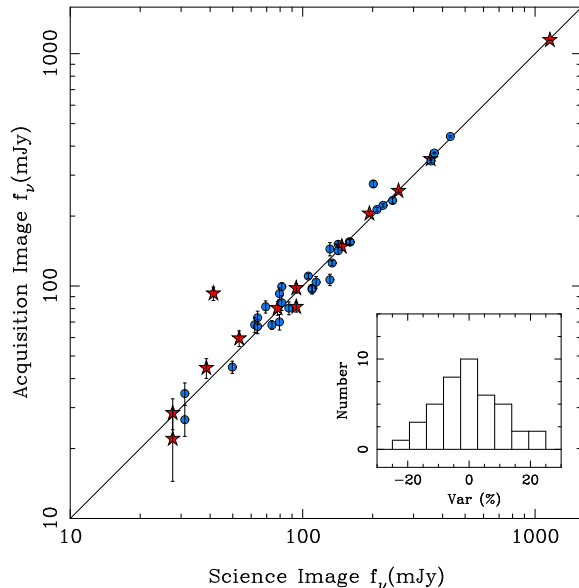


**Figure 4.** Comparison between the 8.7  $\mu\text{m}$  nuclear aperture photometry on the CanariCam science images and the acquisition images for the spectroscopy using a 2 arcsec-diameter aperture. The star symbols represent galaxies for which the CanariCam science images were affected by pattern noise or had distorted PSF (see Table 2), whereas the circles are the rest of the galaxies in the sample. The solid line is not a fit but the 1:1 relation. For clarity we only show the errors on the acquisition image photometry, which are larger than on the science image photometry, as calculated using Equation 3 (see text for details). The inset shows the variation computed as the difference for a given galaxy of the two flux densities divided by the average of the two.

Table 3 summarizes the details of the spectroscopic observations including the date of the observation, on-source time and number of repetitions, PA of the slit, and the name of the standard star and measured FWHM (see below). For reference the last column of this table specifies if the spectroscopic observations of the galaxy have already been published by us. Since all the spectroscopic observations in the ESO/GTC large program were obtained from 2013 March onwards, they are not affected by the noise introduced by the SIR1-CR readout mode (see Section 3.1).

We also used REDCAN (González-Martín et al. 2013) to reduce the CanariCam spectroscopy. The first three steps of the data reduction are the same as for the imaging, then REDCAN performs the two-dimensional wavelength calibration of the galaxy and standard star spectra using sky lines. Finally, the trace determination needed for the extracting the one-dimensional (1D) spectra is done using the standard star data. The last steps of the data reduction are the spectral extraction and the correction for slit losses for point sources. For the final steps it is necessary to determine whether the nuclear emission is unresolved or extended. This analysis is done in the next section and the extraction of the 1D spectra and analysis are presented in Section 3.5.

For the spectroscopic observations we estimated the angular resolution of the data from the FWHM of the standard star acquisition images. The measured values for the CanariCam spectroscopy are given Table 3 and plotted in Fig. 2. The median value of the FWHM of the spectroscopic obser-

**Table 3.** Log of the GTC/CanariCam spectroscopic observations.

Galaxy	Date (yyyy-mm-dd)	$t_{\text{on}} \times \text{rep}$ (s)	PA (degree)	Star	FWHM (arcsec)	Ref
3C273	2014-03-17	$354 \times 3$	0	HD 107328	0.42	
3C382	2013-08-29	$943 \times 1$	0	HD 176670	0.28	
3C390.3	2013-08-26	$354 \times 2$	0	HD 158996	0.49	
IRAS 08572+3915	2013-03-16	$354 \times 3$	0	HD 83787	0.24	
IRAS 13197-1627	2015-03-02	$943 \times 1$	90	HD 116879	0.31	
IRAS 13349+2438	2014-06-15	$943 \times 1$	0	HD 121710	0.31	
IRAS 14348-1447	2015-03-16	$1179 \times 2$	25	HD 130157	0.47	
IRAS 17208-0014	2013-09-09	$1238 \times 1$	90	HD 157999	0.30	
Mrk 3	2014-11-06	$943 \times 1$	30	HD 34450	0.25	
Mrk 231	2014-03-13	$354 \times 2$	290	HD 111335	0.28	
Mrk 463	2014-03-18	$177 \times 3$	82	HD 125560	0.50	
Mrk 478	2014-06-07	$1238 \times 1$	0	HD 128902	0.30	
	2014-06-07	$1238 \times 1$	0	HD 128902	0.26	
Mrk 841	2014-05-27	$943 \times 1$	0	HD 133165	0.37	
	2014-05-01	$943 \times 1$	0	HD 133165	0.28	
Mrk 1014	2013-09-09	$1238 \times 2$	0	HD 10550	0.28	
Mrk 1066	2013-08-31	$354 \times 3$	315	HD 18449	0.28	1, 2
Mrk 1073	2013-09-10	$413 \times 3$	75	HD 14146	0.34	1
Mrk 1210	2014-12-04	$295 \times 3$	0	HD 66141	0.27	
Mrk 1383	2014-05-19	$943 \times 1$	0	HD 126927	0.34	
	2014-06-09	$943 \times 1$	0	HD 126927	0.30	
NGC 931	2013-09-16	$354 \times 3$	80	HD 14146	0.33	
NGC 1194	2013-09-06	$295 \times 3$	310	HD 20356	0.34	
NGC 1275	2013-09-09	$354 \times 3$	0	HD 19476	0.27	
NGC 1320	2013-09-06	$295 \times 3$	315	HD 20356	0.34	
NGC 1614	2014-01-05	$1242 \times 1$	90	HD 28749	0.64	3
	2013-09-08	$1242 \times 1$	0	HD 28749	0.45	
NGC 2273	2013-09-22	$354 \times 1$	290	HD 42633	0.32	1
	2013-09-23	$295 \times 3$	290	HD 42633	0.26	1
NGC 2992	2014-02-14	$943 \times 1$	30	HD 82660	0.30	4
NGC 3227	2014-12-03	$943 \times 1$	0	HD 85503	0.35	
NGC 4051	2014-02-09	$354 \times 3$	310	HD 95212	0.42	
NGC 4253	2014-03-17	$354 \times 3$	285	HD 108381	0.27	
NGC 4258	2015-02-04	$1238 \times 1$	325	HD 107274	0.26	
NGC 4388	2015-03-07	$943 \times 1$	90	HD 111067	0.58	
NGC 4419	2015-02-17	$1238 \times 1$	310	HD 109511	0.41	
NGC 4569	2015-02-06	$1238 \times 2$	30	HD 111067	0.43	
NGC 4579	2015-02-12	$1238 \times 1$	55	HD 111067	0.29	
NGC 5347	2014-06-11	$943 \times 1$	283	HD 121710	0.32	
NGC 5548	2014-06-10	$1061 \times 1$	0	HD 127093	0.32	
NGC 5793	2015-03-02	$943 \times 1$	315	HD 133774	0.30	
NGC 6240	2013-09-15	$1238 \times 1$	16	HD 157999	0.40	1, 5
NGC 7465	2013-08-30	$943 \times 1$	330	HD 220363	0.29	
	2013-08-29	$295 \times 3$	330	HD 220363	0.26	
OQ208	2014-06-09	$943 \times 1$	0	HD 127093	0.28	
	2014-06-06	$354 \times 3$	0	HD 127093	0.25	
PG 0804+761	2014-01-03	$354 \times 3$	0	HD 64307	0.33	
	2014-03-15	$354 \times 3$	0	HD 64307	0.33	
PG 0844+349	2014-12-05	$1238 \times 1$	0	HD 81146	0.35	
	2014-12-03	$1238 \times 1$	0	HD 81146	0.28	
PG 1211+143	2014-03-14	$294 \times 3$	0	HD 113996	0.34	
	2014-06-18	$943 \times 1$	0	HD 109511	0.24	
PG 1229+204	2014-06-09	$1238 \times 1$	0	HD 111067	0.35	
	2014-06-20	$1238 \times 1$	0	HD 111067	0.42	
PG 1411+442	2014-05-30	$1238 \times 1$	0	HD 128902	0.42	
	2014-05-31	$1238 \times 1$	0	HD 128902	0.36	
UGC 5101	2014-01-06	$1242 \times 1$	90	HD 79354	0.33	6

*Notes.* The references listed in the last column indicate previous works where the galaxies have been presented. 1. Alonso-Herrero et al. (2014). 2. Ramos Almeida et al. (2014b). 3. Pereira-Santaella et al. (2015). 4. García-Bernete et al. (2015). 5. Mori et al. (2014). 6. Martínez-Paredes et al. (2015).



**Table 4.** Aperture photometry on the GTC/CanariCam 8.7  $\mu\text{m}$  images.

Galaxy	FWHM (arcsec)	Flux densities (mJy)		
		1arcsec	2arcsec	Unresolved
3C273	0.30	188.0 $\pm$ 0.6	221.7 $\pm$ 1.5	236
3C382	0.23	60.3 $\pm$ 0.8	69.3 $\pm$ 1.8	74
3C390.3	0.30	80.4 $\pm$ 0.6	95.9 $\pm$ 1.3	102
IRAS 08572+3915 North	0.28	358.9 $\pm$ 0.8	431.8 $\pm$ 1.7	460
IRAS 13197–1627	0.36	274.7 $\pm$ 0.9	355.1 $\pm$ 2.0	
IRAS 13349+2438	0.28	314.2 $\pm$ 0.8	356.3 $\pm$ 1.9	379
IRAS 14348–1447 North	...	12.1 $\pm$ 0.8	17.7 $\pm$ 1.9	
IRAS 14348–1447 South	0.43	28.2 $\pm$ 0.8	40.5 $\pm$ 1.9	
IRAS 17208–0014	0.53	57.9 $\pm$ 0.5	109.7 $\pm$ 1.1	
Mrk 3	0.74	110.4 $\pm$ 0.8	201.2 $\pm$ 1.8	227
Mrk 231	0.42	802.4 $\pm$ 0.8	1158.0 $\pm$ 1.9	1273
Mrk 463 East	0.46	186.9 $\pm$ 1.3	258.5 $\pm$ 3.0	284
Mrk 478	0.28	50.4 $\pm$ 0.5	62.2 $\pm$ 1.2	65
Mrk 841	0.30	72.8 $\pm$ 0.6	87.2 $\pm$ 1.3	93
Mrk 1014	0.51	27.8 $\pm$ 0.5	41.3 $\pm$ 1.1	47
Mrk 1066	0.30	82.3 $\pm$ 0.7	142.2 $\pm$ 1.7	
Mrk 1073	0.33	62.1 $\pm$ 0.6	109.8 $\pm$ 1.4	
Mrk 1210	0.32	158.5 $\pm$ 0.6	193.6 $\pm$ 1.5	210
Mrk 1383	0.46	40.0 $\pm$ 0.6	53.3 $\pm$ 1.3	60
NGC 931	0.39	182.9 $\pm$ 0.9	243.7 $\pm$ 2.0	268
NGC 1194	0.33	102.4 $\pm$ 0.6	131.0 $\pm$ 1.4	141
NGC 1275	0.27	314.4 $\pm$ 0.6	368.6 $\pm$ 1.4	396
NGC 1320	0.32	113.7 $\pm$ 0.6	147.4 $\pm$ 1.5	158
NGC 2273	0.30	96.1 $\pm$ 0.7	133.9 $\pm$ 1.7	142
NGC 2992	0.40	51.3 $\pm$ 0.5	78.0 $\pm$ 1.1	
NGC 3227	0.32	150.1 $\pm$ 0.5	208.8 $\pm$ 1.2	225
NGC 4051	0.36	138.4 $\pm$ 0.6	206.2 $\pm$ 1.4	222
NGC 4253	0.31	128.8 $\pm$ 0.7	158.8 $\pm$ 1.5	169
NGC 4388	0.37	76.3 $\pm$ 0.7	108.6 $\pm$ 1.6	119
NGC 4419	0.38	45.9 $\pm$ 0.7	73.7 $\pm$ 1.5	
NGC 4569	0.36	28.7 $\pm$ 0.5	49.8 $\pm$ 1.1	
NGC 5347	0.29	91.9 $\pm$ 0.6	114.2 $\pm$ 1.4	121
NGC 5548	0.29	120.3 $\pm$ 0.7	142.2 $\pm$ 1.7	151
NGC 5793	...	18.2 $\pm$ 0.7	47.6 $\pm$ 1.6	
NGC 6240 South	0.38	101.1 $\pm$ 0.6	160.2 $\pm$ 1.3	178
NGC 7465	0.31	25.9 $\pm$ 0.5	38.5 $\pm$ 1.1	41
OQ 208	0.36	58.5 $\pm$ 0.6	79.5 $\pm$ 1.4	86
PG0804+761	0.31	69.1 $\pm$ 0.6	93.8 $\pm$ 1.4	108
PG0844+349	0.35	20.4 $\pm$ 0.6	27.6 $\pm$ 1.4	32
PG1211+143	0.29	67.9 $\pm$ 0.5	81.3 $\pm$ 1.1	86
PG1229+204	0.27	25.8 $\pm$ 0.5	31.1 $\pm$ 1.2	33
PG1411+442	0.27	55.0 $\pm$ 0.6	64.0 $\pm$ 1.3	67
UGC 5101	0.57	54.0 $\pm$ 0.4	105.8 $\pm$ 0.8	

*Notes.*— The apertures are diameters. The quoted errors are calculated according to Equation 3 and do not include the  $\sim 10\%$  uncertainty associated with the photometric calibration (see Section 3.3).

vations is 0.32 arcsec, which is similar to that of the imaging data.

### 3.3 Aperture Photometry

We performed aperture photometry on the CanariCam 8.7  $\mu\text{m}$  images using IRAF<sup>4</sup> routines. The nuclear 8.7  $\mu\text{m}$

flux densities (without the correction for point source emission) measured through different apertures are given in Table 4. The background in the sky-subtracted images was measured in an annulus with an inner radius of 30 pixels (2.4 arcsec) and a 5 pixel width, except for the very extended sources where we used an annulus with a radius of 45 pixels (3.6 arcsec).

We list in Table 4 the errors in the photometry due to the background subtraction uncertainty, which are computed as follows (see e.g. Reach et al. 2005). The first term is associated to the annulus used for the background subtraction:

$$\sigma_{\text{sky}} = S_{\text{sky}} N_{\text{on}} / \sqrt{N_{\text{sky}}} \tag{1}$$

<sup>4</sup> IRAF is distributed by the National Optical Astronomy Observatory, which is operated by the Association of Universities for Research in Astronomy (AURA) under cooperative agreement with the National Science Foundation.

where  $S_{\text{sky}}$  is the standard deviation of the sky annulus,  $N_{\text{on}}$  is the number of pixels in the on-source photometric aperture, and  $N_{\text{sky}}$  is the number of pixels in the sky annulus. The second term accounts for noise due to sky variations within the on-source aperture which can be expressed as:

$$\sigma_{\text{sky,on}} = S_{\text{sky}} \sqrt{N_{\text{on}}} \quad (2)$$

The total error is then calculated by summing these two terms in quadrature:

$$\sigma_{\text{tot}} = \sqrt{\sigma_{\text{sky}}^2 + \sigma_{\text{sky,on}}^2} \quad (3)$$

Additionally, the typical errors associated with the photometric calibration in the  $N$ -band window are usually estimated to be approximately 10 – 15%. For our large data set we can compare the aperture photometry done on the science images (i.e., those presented in Section 3.1) and on the shorter integration time acquisition images taken for the spectroscopy. Since in the majority of cases the galaxy images were taken on different nights, this comparison can give an estimate of the uncertainties in the photometric calibration. To make this comparison we chose the fluxes measured within a 2 arcsec-diameter aperture to avoid the added uncertainty of the point source correction for point-like sources while keeping the uncertainties due to the background subtraction low. We present the comparison in Fig. 4. In this figure we only show the errors on the aperture photometry on the acquisition images because the sky-subtracted image backgrounds have a higher standard deviation due to the shorter integration times.

As can be seen from this figure, the agreement in the photometry is excellent. The most discrepant point in Fig. 4 is Mrk 1014 for which the flux density measured on the CanariCam acquisition image is approximately twice that on the science image. Comparison with the nuclear photometry of this source presented in Asmus et al. (2014) indicates that the flux measured on the CanariCam science image is the correct one. We cannot, however, rule out variability. The inset of Fig. 4 shows the distribution of the variation in the photometry for each galaxy, computed as the difference between the two measurements divided by the average of the two. The standard deviation of this distribution (excluding Mrk 1014) is 11%. We also marked in Fig. 4 as star symbols those CanariCam science observations affected by pattern noise or had distorted PSFs (see Table 2, last column). We do not see a clear trend for the most discrepant photometric points to be related to these issues.

A detailed comparison of our nuclear fluxes with other works presenting photometry for large number of AGNs (e.g., Gorjian et al. 2004; Asmus et al. 2014) is not straightforward because of the different  $N$ -band filters and methods used to determine the nuclear fluxes as well as possible variability in the mid-IR.

We measured the size of the nuclear regions before rotating and smoothing the GTC/CanariCam 8.7  $\mu\text{m}$  images (Section 3.1) by fitting a moffat function to the nuclear emission. The measured sizes (FWHM) of the nuclear mid-IR emission in arcseconds for the nuclear regions of the AGN are listed in Table 4. For those galaxies with nuclear FWHMs similar to those of their corresponding standard stars and no clear diffuse extended emission we also estimated the unresolved nuclear fluxes. To do so, we used the fluxes measured

through the smallest aperture and estimated the aperture correction for the total flux using the standard star observations. We note that the unresolved nuclear fluxes estimated using this method (see Table 4) are likely to be slightly overestimated as there is always a small fraction of resolved emission from the galaxy even in the smallest aperture. We will present a detailed analysis of the CanariCam unresolved emission of AGN using PSF-scaling photometry in García-Bernete et al. (2016, in preparation).

### 3.4 Extraction and flux calibration of the spectra

Before we extracted the 1D spectra we compared the measured nuclear sizes of the galaxies with the FWHM of their corresponding standard stars. We used this comparison to decide the type of extraction. The second column of Table 5 specifies whether the spectrum was extracted as a point source or as an extended source. In the latter case we give the extraction aperture in arcseconds. In the case of point source extraction, REDCAN uses an extraction aperture that increases with wavelength to account for the decreasing diffraction-limited angular resolution and performs an additional correction for slit losses. For those galaxies with double nuclei detected in the mid-IR, we only present in this work that corresponding to the brightest nucleus.

For the nuclear spectra extracted as point sources we compared the flux density 8.7  $\mu\text{m}$  in the 1D flux-calibrated spectra with the unresolved fluxes estimated from the 8.7  $\mu\text{m}$  CanariCam images (see Table 4). In most cases the 8.7  $\mu\text{m}$  fluxes agreed to within 25%. When the discrepancy was large we scaled the extracted 1D spectra to the imaging data unresolved fluxes estimated at 8.7  $\mu\text{m}$  (Section 3.3). In the case of the extracted spectra for NGC 1614 along the two slit PA (north-south, PA=0 degrees and east-west, PA=90 degrees), we simulated the slit on the acquisition image to flux calibrate the spectra. In the cases where there were more than one repetition or spectroscopic observations taken on different nights we combined the individual flux calibrated spectra.

### 3.5 Analysis of the spectra

Figure 5 shows the fully reduced and flux calibrated 1D CanariCam spectra of the 45 AGN in the ESO/GTC program. We smoothed the 1D CanariCam spectra by using a moving average of five spectral points. We computed the errors as the standard deviation of the flux densities in these narrow wavelength bins. We note that this approach overestimates the errors of the emission lines and PAH features. We mark in this figure the most important emission lines and PAH features.

We measured the mid-IR spectral index in the CanariCam spectra, defined as  $f_{\nu} \propto \nu^{\alpha_{\text{MIR}}}$ , using the flux ratios at the approximate end points of the spectra. These wavelengths are typically 8 and 12.5  $\mu\text{m}$  (rest-frame) for the Seyferts and LLAGN, and 7.5 and 12  $\mu\text{m}$  for the more distant AGN (see Table 5). For each galaxy we chose them visually to avoid end wavelength points strongly affected by low atmospheric transmission.

The strength of the silicate feature is computed as  $S_{\text{Si}} = \ln(f_{\text{cont}}/f_{\text{feature}})$ , where  $f_{\text{cont}}$  is the continuum at the

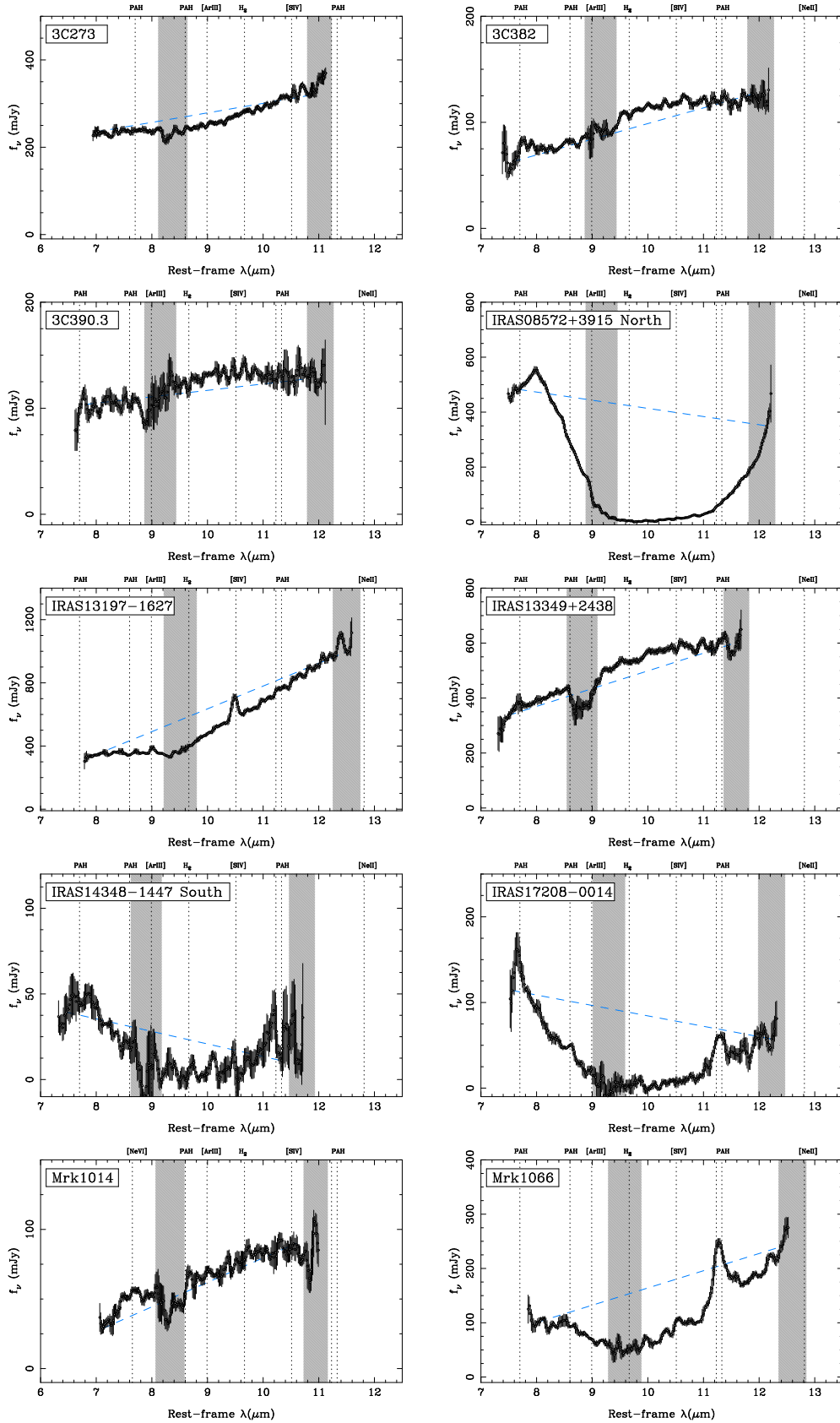


**Figure 5.** Flux-calibrated GTC/CanariCam 1D spectra (see Section 3.4 for details) of the 45 AGN in the ESO/GTC sample. The dashed blue line is the continuum fit (see text for details). The shaded areas represent spectral ranges of low atmospheric transmission and highly variable emission especially near  $9.5 \mu\text{m}$  due the ozone at El Roque de los Muchachos observatory.

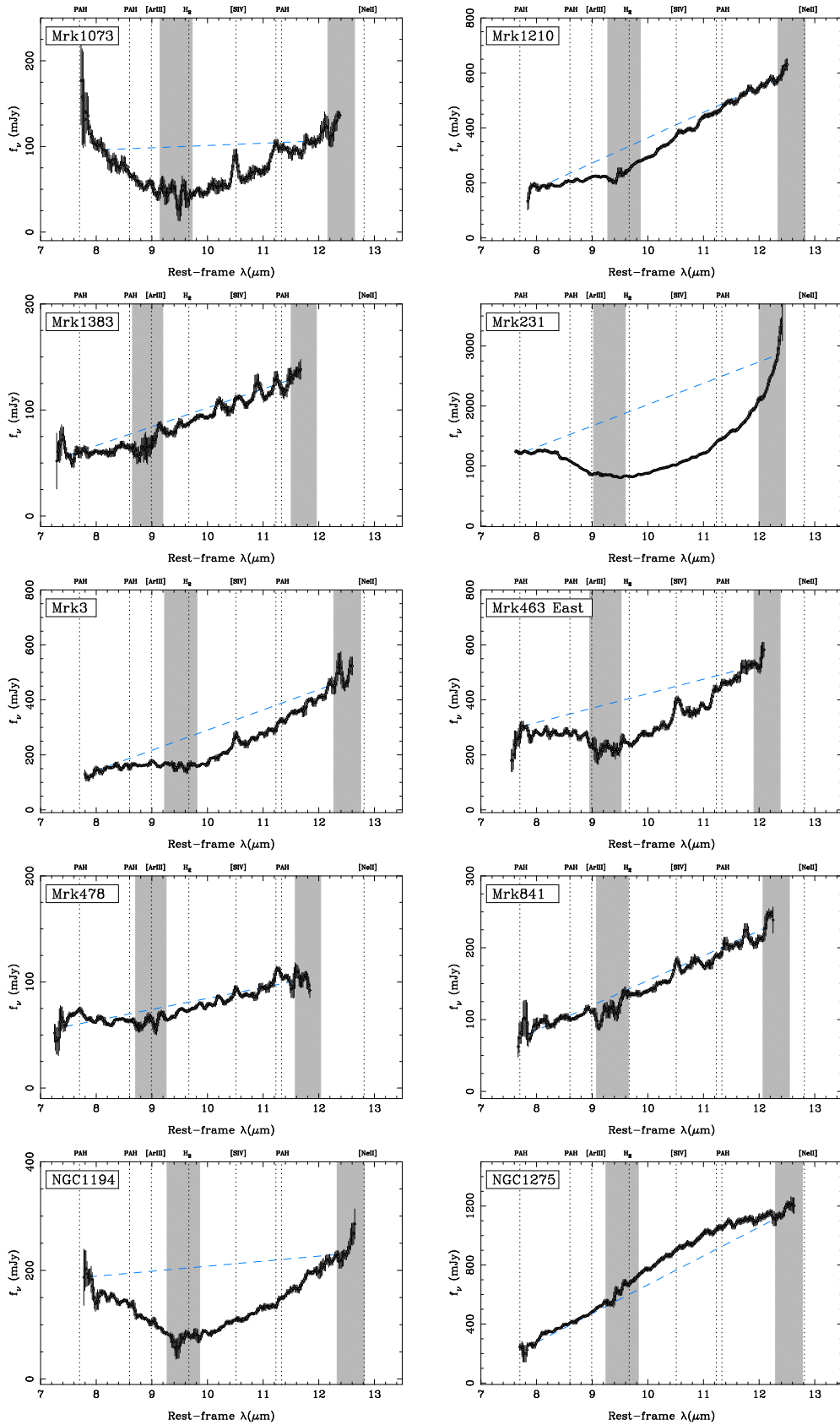


Figure 5. Continued.

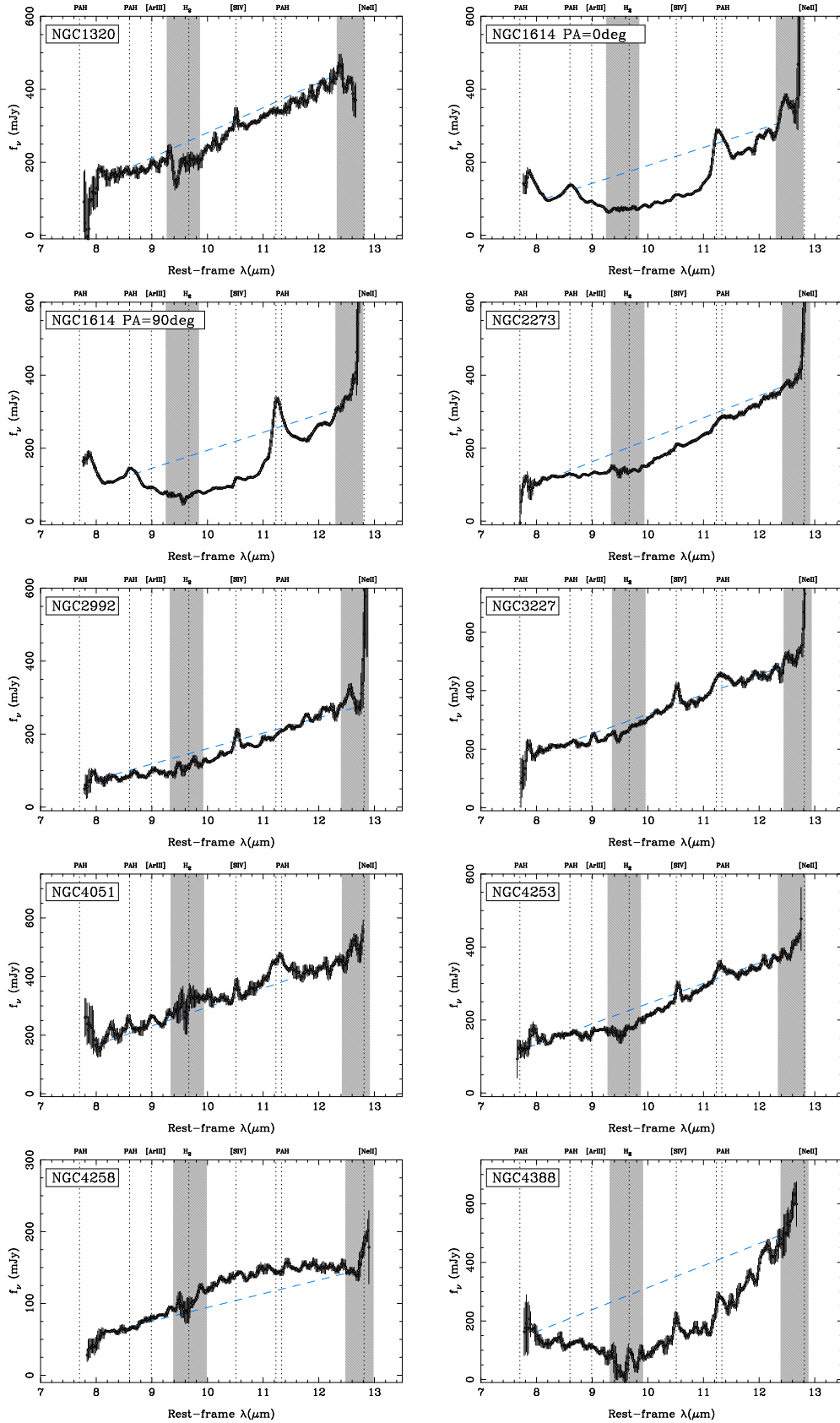


Figure 5. Continued.

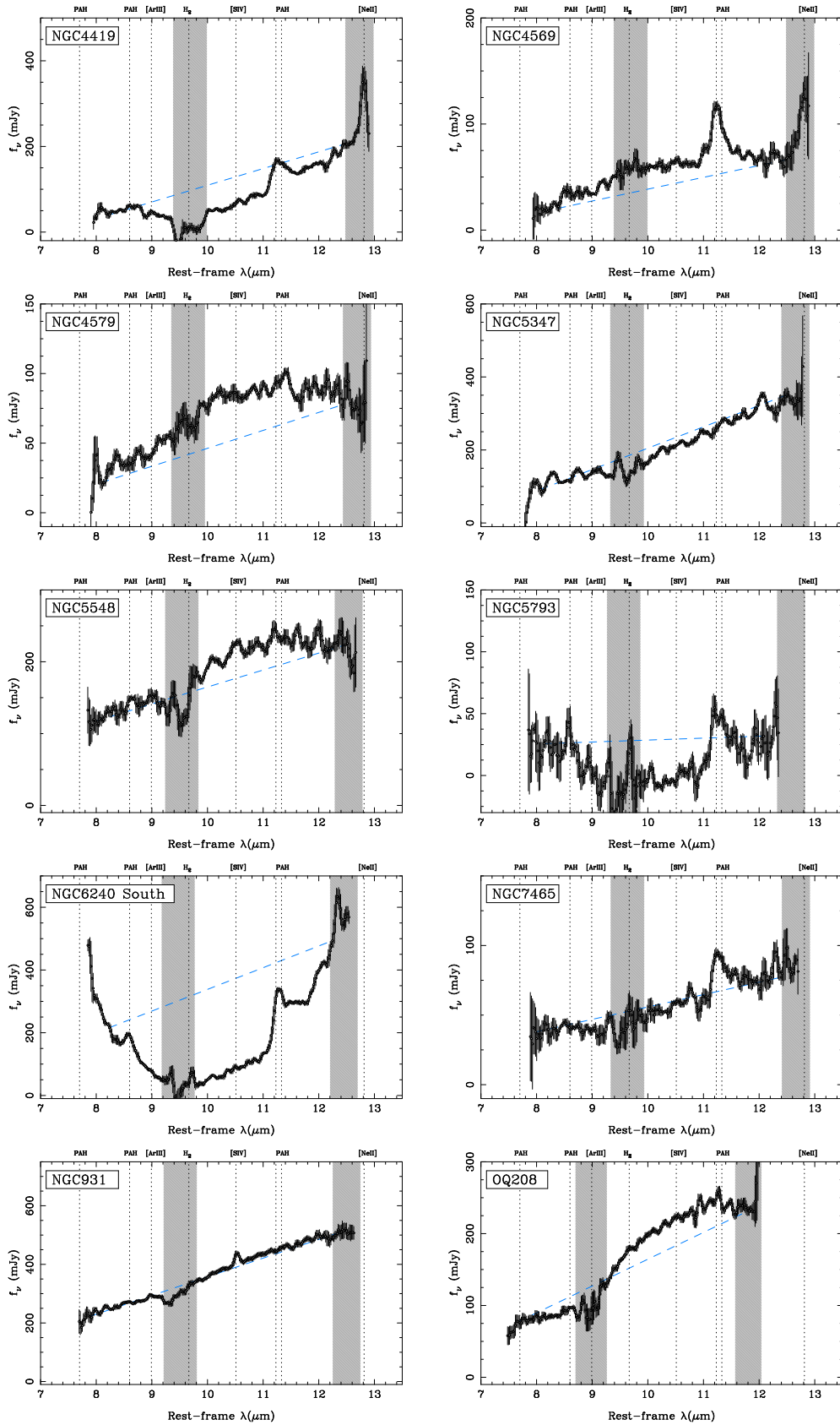


Figure 5. Continued.

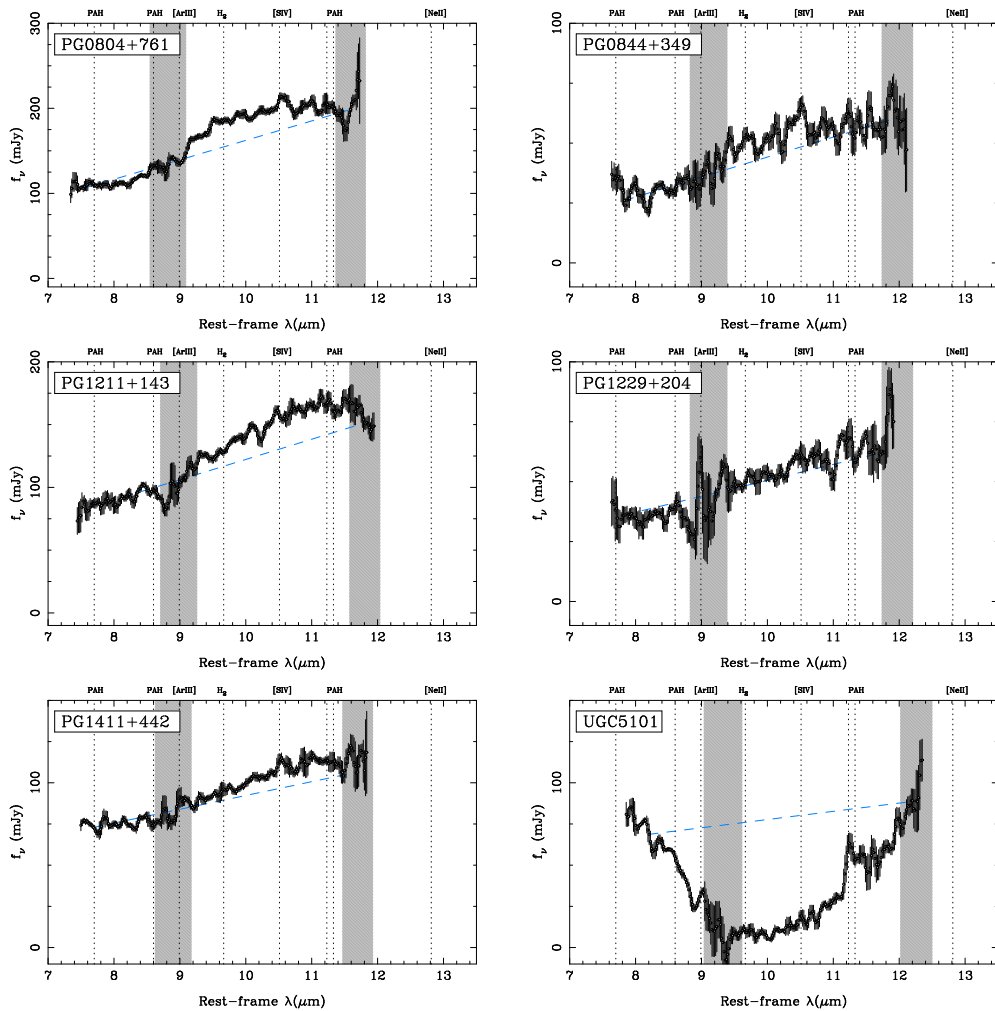


Figure 5. Continued.

wavelength of the feature and  $f_{\text{feature}}$  is the flux density of the feature, which we evaluated at rest-frame  $9.7 \mu\text{m}$ . The only exception was NGC 4419 for which we evaluated them at  $10 \mu\text{m}$  to avoid the bad ozone residual in the spectrum at  $9.7 \mu\text{m}$  rest-frame (see Fig. 5). We fitted the continuum as a straight line between the same wavelengths used to measure the spectral index.

In nuclei with strong PAH emission it is difficult to estimate the continuum given the relatively narrow spectral range attained from the ground. In those cases we placed the blue end of the continuum in between the  $7.7$  and  $8.6 \mu\text{m}$  PAH features (see e.g., NGC 6240 South or NGC 1614 in Fig. 5). Similarly, for AGN with deep silicate absorption features it is difficult to measure the underlying continuum and therefore the resulting measured strength could be significantly underestimated.

To estimate the uncertainties in the measured spectral index we performed Monte Carlo simulations allowing the flux densities at the end wavelengths to vary within their estimated errors. We then computed the average and the standard deviation of these simulations that are listed in Table 5. For the strength of the silicate feature we again performed Monte Carlo simulations allowing the flux of the feature to vary within the measured errors to estimate the uncertainty

in the measurement. For NGC 5793 and IRAS 17208–0014 we were not able to estimate the uncertainty in the strength of the silicate feature because the uncertainties of the flux density at  $9.7 \mu\text{m}$  allow for negative values.

Those AGN in our sample with the silicate feature in emission do not show the peak at  $9.7 \mu\text{m}$  but rather at longer wavelengths. From Fig. 5 we can see that the peak is usually at  $\lambda_{\text{rest}} > 10 \mu\text{m}$ , as also found by e.g. Thompson et al. (2009) and Hatziminaoglou et al. (2015) from *Spitzer*/IRS spectroscopy. However, we measure the strength of the silicate feature at  $9.7 \mu\text{m}$  rest-frame for the comparison with clumpy torus models in Section 4.2. We also measured the strength of the silicate feature in the *Spitzer*/IRS spectra and found that they were consistent within the uncertainties with our CanariCam values. The only exception was NGC 4051, for which the IRS value is consistent with zero or slightly in emission (see also Wu et al. 2009).

For those AGN with bright  $11.3 \mu\text{m}$  PAH feature emission, we measured the equivalent width (EW) of the feature following the method described by Hernán-Caballero & Hatziminaoglou (2011) and Esquej et al. (2014). Briefly, we fitted a local continuum at  $11.25 \mu\text{m}$  by interpolating between two narrow bands on both sides of the feature ( $10.75 - 11.0 \mu\text{m}$  and  $11.65 - 11.9 \mu\text{m}$ ). To obtain the EW

**Table 5.** Spectral measurements.

Galaxy	Extraction	size (pc)	$\lambda_1$ ( $\mu\text{m}$ )	$\lambda_2$ ( $\mu\text{m}$ )	$\alpha_{\text{MIR}}$	$S_{\text{Si}}$	$f_{\nu}(12\ \mu\text{m})$ (mJy)	EW(11.3 $\mu\text{m}$ PAH) ( $\mu\text{m}$ )
3C273	point	1376	7.0	10.8	$-0.66 \pm 0.12$	$-0.02 \pm 0.02$	$317 \pm 6$	no
3C382	point	555	7.6	11.9	$-1.48 \pm 0.34$	$0.15 \pm 0.04$	$123 \pm 7$	
3C390.3	point	541	7.8	11.8	$-0.45 \pm 0.39$	$0.12 \pm 0.07$	$130 \pm 12$	
IRAS 08572+3915 North	point	570	7.7	12.1	$0.66 \pm 0.18$	$-4.41 \pm 0.85$	$76 \pm 9$	
IRAS 13197-1627	point	178	8.0	12.5	$-2.38 \pm 0.07$	$-0.38 \pm 0.02$	$859 \pm 33$	
IRAS 13349+2438	point	991	7.5	11.6	$-1.34 \pm 0.16$	$0.11 \pm 0.02$	$585 \pm 20$	no
IRAS 14348-1447 South	point	786	7.5	11.3	$2.98 \pm 1.20$	$-0.88 \pm 0.67$	$20 \pm 12$	no
IRAS 17208-0014	1 arcsec	809	7.6	12.2	$1.39 \pm 0.78$	$-4.07$	$43 \pm 7$	$0.56 \pm 0.07$
Mrk 3	point	137	8.0	12.3	$-2.67 \pm 0.32$	$-0.43 \pm 0.06$	$375 \pm 30$	
Mrk 231	point	420	7.8	12.3	$-1.84 \pm 0.11$	$-0.84 \pm 0.02$	$1592 \pm 32$	
Mrk 463 East	point	499	7.7	11.9	$-1.22 \pm 0.15$	$-0.53 \pm 0.04$	$460 \pm 11$	$< 0.1$
Mrk 478	point	750	7.4	11.7	$-1.25 \pm 0.22$	$-0.08 \pm 0.02$	$96 \pm 5$	no
Mrk 841	point	367	7.9	12.1	$-2.28 \pm 0.52$	$-0.05 \pm 0.03$	$206 \pm 4$	
Mrk 1014	point	1396	7.1	10.6	$-2.78 \pm 0.37$	$0.17 \pm 0.09$	$92 \pm 6$	no
Mrk 1066	point	116	8.0	12.4	$-1.95 \pm 0.20$	$-1.01 \pm 0.14$	$185 \pm 6$	$0.34 \pm 0.02$
Mrk 1073	point	230	8.1	12.2	$-0.23 \pm 0.28$	$-0.76 \pm 0.12$	$91 \pm 6$	$0.08 \pm 0.02$
Mrk 1210	point	146	8.0	12.4	$-2.62 \pm 0.18$	$-0.25 \pm 0.03$	$545 \pm 13$	
Mrk 1383	point	817	7.5	11.5	$-1.87 \pm 0.15$	$-0.07 \pm 0.02$	$112 \pm 3$	no
NGC 931	point	161	7.9	12.4	$-1.78 \pm 0.25$	$0.00 \pm 0.03$	$486 \pm 10$	
NGC 1194	point	132	7.9	12.5	$-0.40 \pm 0.19$	$-0.94 \pm 0.07$	$196 \pm 4$	
NGC 1275	point	173	8.0	12.3	$-3.20 \pm 0.18$	$0.13 \pm 0.03$	$1109 \pm 22$	
NGC 1320	point	85	8.2	12.3	$-2.43 \pm 0.39$	$-0.18 \pm 0.10$	$393 \pm 20$	
NGC 1614 (PA=90 deg)	2 arcsec	131	8.2	12.3	$-2.63 \pm 0.10$	$-0.89 \pm 0.10$	$226 \pm 9$	$0.39 \pm 0.02$
NGC 1614 (PA=0 deg)	2 arcsec	131	8.2	12.3	$-2.69 \pm 0.22$	$-0.87 \pm 0.06$	$238 \pm 5$	$0.29 \pm 0.01$
NGC 2273	point	64	8.0	12.6	$-2.85 \pm 0.16$	$-0.39 \pm 0.04$	$315 \pm 8$	$0.033 \pm 0.005$
NGC 2992	point	90	8.1	12.7	$-2.75 \pm 0.24$	$-0.19 \pm 0.10$	$239 \pm 8$	
NGC 3227	point	51	8.0	12.6	$-2.12 \pm 0.15$	$-0.07 \pm 0.04$	$462 \pm 9$	$0.065 \pm 0.005$
NGC 4051	point	32	8.0	12.5	$-2.18 \pm 0.37$	$0.25 \pm 0.09$	$408 \pm 13$	$0.095 \pm 0.009$
NGC 4253	point	141	7.8	12.5	$-2.25 \pm 0.44$	$-0.23 \pm 0.03$	$342 \pm 11$	$0.060 \pm 0.006$
NGC 4258	point	22	8.1	12.6	$-1.96 \pm 0.30$	$0.16 \pm 0.07$	$150 \pm 5$	
NGC 4388	point	43	8.0	12.5	$-2.47 \pm 0.50$	$-1.11 \pm 0.20$	$344 \pm 19$	
NGC 4419	point	43	8.3	12.5	$-3.52 \pm 0.25$	$-0.77 \pm 0.14$	$190 \pm 5$	$0.21 \pm 0.01$
NGC 4569	1 arcsec	82	8.1	12.5	$-3.00 \pm 0.87$	$0.53 \pm 0.07$	$68 \pm 3$	$0.30 \pm 0.02$
NGC 4579	point	43	8.1	12.4	$-2.75 \pm 0.61$	$0.40 \pm 0.07$	$93 \pm 7$	
NGC 5347	point	87	8.1	12.5	$-2.94 \pm 0.42$	$-0.27 \pm 0.04$	$307 \pm 10$	
NGC 5548	point	181	8.0	12.5	$-1.36 \pm 0.33$	$0.13 \pm 0.15$	$220 \pm 15$	
NGC 5793	2 arcsec	126	8.1	12.1	$-0.65 \pm 1.06$	$-0.39$	$14 \pm 3$	$\sim 1$
NGC 6240 South	point	247	8.2	12.2	$-2.05 \pm 0.21$	$-1.49 \pm 0.39$	$297 \pm 7$	$0.27 \pm 0.02$
NGC 7465	point	55	8.0	12.4	$-1.38 \pm 0.98$	$0.04 \pm 0.24$	$74 \pm 4$	$0.16 \pm 0.02$
OQ 208	point	731	7.7	11.8	$-2.45 \pm 0.27$	$0.17 \pm 0.02$	$247 \pm 5$	no
PG 0804+761	point	922	7.5	11.6	$-1.46 \pm 0.14$	$0.19 \pm 0.02$	$203 \pm 4$	no
PG 0844+349	point	621	7.8	12.0	$-2.00 \pm 0.64$	$0.28 \pm 0.06$	$57 \pm 11$	
PG 1211+143	point	772	7.6	11.8	$-1.29 \pm 0.21$	$0.12 \pm 0.03$	$171 \pm 8$	no
PG 1229+204	point	615	7.8	11.8	$-1.36 \pm 0.36$	$0.11 \pm 0.06$	$68 \pm 9$	
PG 1411+442	point	840	7.7	11.7	$-0.98 \pm 0.23$	$0.07 \pm 0.03$	$116 \pm 3$	no
UGC 5101	1 arcsec	755	8.2	12.3	$-0.74 \pm 0.55$	$-1.88 \pm 0.35$	$46 \pm 11$	$0.21 \pm 0.03$

*Notes.* The second column indicates the type of spectral extraction, while the third column is the physical size of the slit for unresolved sources or the extraction aperture for extended sources.  $\lambda_1$  and  $\lambda_2$  are the rest-frame wavelengths between which we fitted the continuum as well as the end points to compute the mid-IR spectral index  $\alpha_{\text{MIR}}$ . The nuclear  $12\ \mu\text{m}$  flux densities are in observed frame and the quoted errors only include the dispersion of the spectra (see Section 3.5) but not the additional 10% photometric calibration uncertainty. In the last column 'no' indicates those nuclei for which the rest-frame spectral range does not cover the  $11.3\ \mu\text{m}$  PAH feature or the continuum next to the  $11.3\ \mu\text{m}$  PAH feature.

we divided the flux of the feature integrated in the spectral range  $11.05 - 11.55\ \mu\text{m}$  by the fitted continuum and corrected it for the missing flux (see Hernán-Caballero & Hatziminaoglou 2011, for full details). We estimated the uncertainties in the EW as the dispersion around the measured fluxes and EWs in 100 Monte Carlo simulations of the original spectrum with random noise distributed as the rms of the CanariCam spectrum. We note that PAH fluxes, and

thus EW, obtained with a local continuum are lower (typically by a factor of two) than those using a continuum fitted over a broad spectral range (e.g. with PAHFIT, see Smith et al. 2007).

In Table 5 we list for each galaxy the rest-frame wavelengths used to compute the spectral index, the spectral index and the strength of the silicate feature with the corresponding uncertainties, the observed nuclear  $12\ \mu\text{m}$  flux



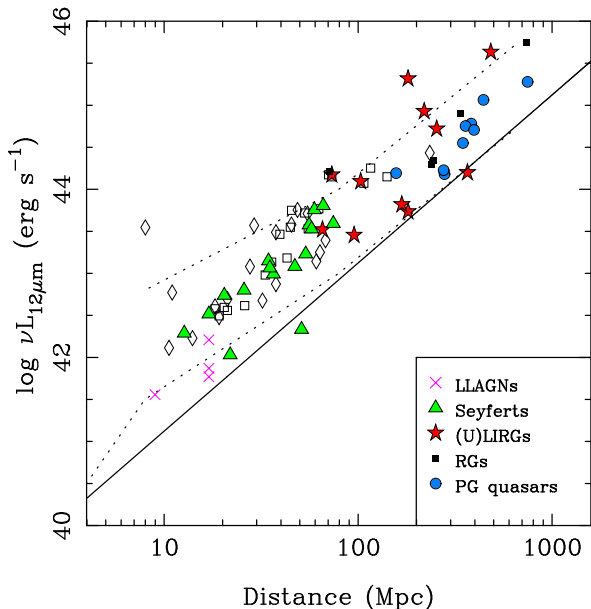


**Figure 6.** Nuclear rest-frame monochromatic  $12\ \mu\text{m}$  luminosity against the luminosity distance for the 45 AGN in the ESO/GTC large program. The color symbols indicate the different AGN classes in our sample. The diamonds and squares are AGN (mostly Seyferts and LIRGs) with Gemini/T-ReCS spectroscopy from González-Martín et al. (2013) and VLT/VISIR spectroscopy from Hönig et al. (2010), respectively. The dotted lines delineate approximately the location of the AGN in the mid-IR imaging atlas of Asmus et al. (2014). The solid line shows a constant flux density of  $45\ \text{mJy}$  at  $12\ \mu\text{m}$  (see Section 4.1).

densities from the spectra and for those nuclei with clear  $11.3\ \mu\text{m}$  PAH emission, the EW of the feature. We also list in this table the physical sizes probed by the slit width, that is, the physical scale corresponding to  $0.52\ \text{arcsec}$  for point source spectra, and the optimized extraction aperture for extended sources. The median physical sizes probed by the CanariCam spectroscopy are approximately  $90\ \text{pc}$  for the Seyferts and LLAGN and  $640\ \text{pc}$  for the rest of the sample.

Finally, we estimated the nuclear rest-frame  $12\ \mu\text{m}$  luminosities of our sample of AGN from the CanariCam 1D flux-calibrated spectra. For the most distant sources in our sample, these were extrapolated from the fitted continuum to the observed CanariCam spectra (see above).

## 4 NUCLEAR MID-IR SPECTROSCOPIC PROPERTIES OF LOCAL AGN

### 4.1 Nuclear $12\ \mu\text{m}$ emission

The nuclear mid-IR continuum of AGN and in particular the monochromatic  $12\ \mu\text{m}$  nuclear emission are believed to be a good proxy for the AGN luminosity. This is based on the good correlation found between the AGN hard X-ray (absorption corrected) luminosity and the  $12\ \mu\text{m}$  emission over four orders of magnitude (Levenson et al. 2009; Gandhi et al. 2009; Asmus et al. 2011; Mason et al. 2012). Moreover, these works found that the  $12\ \mu\text{m}$  nuclear emission of type 1 and type 2 AGN is not significantly different (although see Yan et al. 2015; Burtscher et al. 2015). This has been

explained in the context of the mild anisotropy of the mid-IR emission vs. e.g. the viewing angle predicted by clumpy torus models and smooth dusty torus models (see e.g. Horst et al. 2008; Nenkova et al. 2008; Levenson et al. 2009; Hönig & Kishimoto 2010; Feltre et al. 2012; Yan et al. 2015).

It is interesting to compare the nuclear  $12\ \mu\text{m}$  luminosities of our sample with the sub-arcsecond mid-IR imaging compilation of 253 AGN presented by Asmus et al. (2014). This way we can determine if our spectroscopic sample is representative of the local population of mid-IR *bright* AGN. In Fig. 6 we plot the nuclear rest-frame monochromatic  $12\ \mu\text{m}$  luminosity against the distance for the 45 AGN in the ESO/GTC large program. This figure can be compared directly with figure 13 of Asmus et al. (2014), although we note that they used a slightly different cosmology ( $H_0 = 63\ \text{km s}^{-1}\ \text{Mpc}^{-1}$ ). We show in our figure the approximate location of the Asmus et al. (2014) AGN with unresolved  $12\ \mu\text{m}$  emission as dotted lines. We also show the line of constant  $12\ \mu\text{m}$  flux density of  $45\ \text{mJy}$ . This value is expected from the approximate flux limit of our sample of  $25\ \text{mJy}$  at  $8.7\ \mu\text{m}$  for spectroscopy and the median spectral index of the sample  $\alpha_{\text{MIR}} = -2$  (see Table 5). The comparison with the imaging compilation of Asmus et al. (2014) demonstrates that, when compared to the imaging atlas, our spectroscopic atlas at a given distance is not biased towards the most luminous mid-IR AGN.

The nuclear  $12\ \mu\text{m}$  luminosities of our sample cover over four orders of magnitude. According to the mid-IR vs. X-ray correlation, our sample would probe four orders of magnitude of AGN luminosity, as also shown in Fig. 1. The PG quasars, (U)LIRGs and RGs have a median  $\log(\nu L_{12\ \mu\text{m}}/\text{erg s}^{-1}) = 44.3$ , whereas the Seyferts and LLAGN have  $\log(\nu L_{12\ \mu\text{m}}/\text{erg s}^{-1}) = 43$ . We note that two LLAGN in our sample (NGC 4419 and NGC 4569) show bright PAH emission in their nuclear CanariCam spectra (see Fig. 5 and also Section 4.3). Thus their  $12\ \mu\text{m}$  luminosities might be dominated by emission related to star formation activity as found in a few LLAGN (see e.g. Mason et al. 2012; Asmus et al. 2014; González-Martín et al. 2015).

We also plot in Fig. 6 a sample of AGN (mostly Seyferts and LIRGs) with sub-arcsecond resolution Gemini/T-ReCS spectroscopy taken from the work of González-Martín et al. (2013) and VLT/VISIR spectroscopy from Hönig et al. (2010). The Seyfert galaxies observed in our ESO/GTC large program occupy a similar region in this diagram as the previously published sub-arcsecond mid-IR spectroscopy. Notably, however, our ESO/GTC large program also extends the existing sub-arcsecond mid-IR spectroscopy to more luminous and distant AGN, namely, ULIRGs (see also Soifer et al. 2002), PG quasars, and RGs.

### 4.2 Mid-IR spectral index and the $9.7\ \mu\text{m}$ silicate feature

In this section we discuss two quantities that provide a simple description of the ground-based mid-IR spectrum of an AGN, namely the spectral index and the strength of the silicate feature (see Section 3.5).

In the cases of relatively featureless spectra the spectral index gives an estimate of the shape of the AGN mid-IR continuum, which can be compared with clumpy torus model predictions (see below and also Ramos Almeida et al.

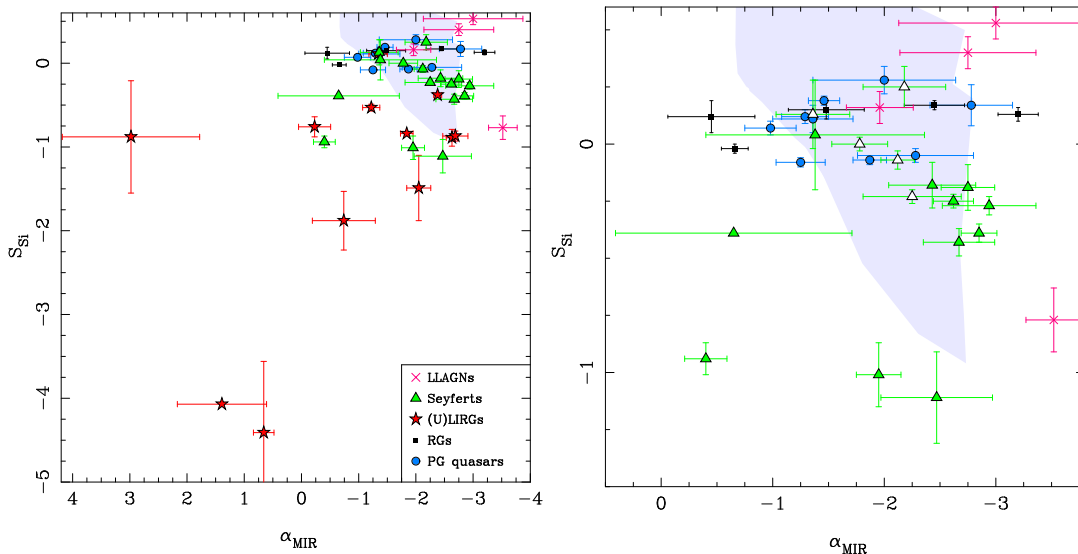


**Figure 7.** *Left panel.* Nuclear  $\alpha_{\text{MIR}}$  against the strength of the silicate feature where positive numbers for  $S_{\text{Si}}$  indicate that the feature is in emission and negative numbers in absorption. The shaded area shows the approximate region covered in this diagram by a set of clumpy torus models shown in figure 12 of Hönic et al. (2010). *Right panel.* Same as left but zooming to the region covered by the torus models. Seyfert 1s and 1.5s are plotted as white triangles and Seyfert 1.8s, 1.9s, and 2s as green triangles. We do not show the U(LIRG) nuclei.

2014a; Hönic et al. 2010). The mid-IR spectral indices of the Seyfert galaxies, PG quasars, and RGs in our sample range between  $\alpha_{\text{MIR}} = -0.23$  and  $\alpha_{\text{MIR}} = -3.20$  (see Table 5 and Fig. 7). They are similar to those measured for other Seyfert nuclei using sub-arcsecond 8 to 18  $\mu\text{m}$  imaging data (Ramos Almeida et al. 2011) and VLT/VISIR spectroscopy ( $\alpha_{\text{MIR}} = -1.65 \pm 0.44$  and  $\alpha_{\text{MIR}} = -2.07 \pm 0.54$  for type 1s and 2s, respectively, see Hönic et al. 2010). Buchanan et al. (2006), on the other hand, found from *Spitzer*/IRS spectroscopy (slit widths between 3.6 and 10.7 arcsec) that only 30% of their 12  $\mu\text{m}$  selected sample showed a clear power-law component with spectral indices (measured between 5 and 20  $\mu\text{m}$ ) -0.9 to -2.3. This small fraction is due to an important contribution of star formation and/or diffuse dust emission within the IRS slits.

Four (U)LIRG nuclei in our sample show considerably flatter mid-IR spectral indices ( $\alpha_{\text{MIR}} > -0.5$ ) than the typical values of other AGN. This is in part due to the presence of strong PAH emission at 7.7, 8.6, and 11.3  $\mu\text{m}$ , which makes it difficult to get the intrinsic shape of the AGN continuum. Also in cases of nuclei with deep silicate feature absorption (e.g., IRAS 08572+3915 North, IRAS 17208–0014, UGC 5101), the dust heating source appears to be so embedded that determining the intrinsic mid-IR spectral shape might not be possible unless we perform a spectral decomposition and modeling of the AGN component (see e.g. Martínez-Paredes et al. 2015).

In terms of the silicate feature we can see from Fig. 5 that most PG quasars and RGs as well as three LLAGNs, the ULIRG/Sy1 IRAS 13349+2438 and some Sy1 nuclei show the feature clearly in emission. This is similar to results obtained with *Spitzer*/IRS spectroscopy (see e.g. Shi et al. 2006; Mason et al. 2012). On sub-arcsecond scales most Seyfert nuclei show the feature in moderate absorption or slight emission (see also e.g. Mason et al. 2006, 2009; Hönic et al. 2010; González-Martín et al. 2013; Alonso-Herrero et

al. 2011, 2014). Nuclei in our sample with deep silicate features ( $S_{\text{Si}} \ll -1$ ) are local (U)LIRG indicating that the AGN are likely embedded and obscured by dust not directly associated with the AGN (Levenson et al. 2007; Alonso-Herrero et al. 2011, 2013; González-Martín et al. 2013).

Ramos Almeida et al. (2014a) showed that the nuclear mid-IR spectra of AGN can be used to constrain the number of clouds and optical depth of the clouds of the Nenkova et al. (2008) clumpy torus models. Hönic et al. (2010) used the mid-IR spectral index  $\alpha_{\text{MIR}}$  together with the strength of the silicate feature to also constrain the properties of the Hönic & Kishimoto (2010) torus models. After fixing the width of the torus and the viewing angle, Hönic et al. (2010) used this diagram to constrain the number of clouds and radial distribution of the clouds in their models. They demonstrated however that the mid-IR nuclear spectra do not provide information of the viewing angle of the torus, as also verified by Ramos Almeida et al. (2014a).

Fig. 7 can be compared directly with figure 12 of Hönic et al. (2010) and in the right panel we zoom into the region covered by a subset of the clumpy models of Hönic & Kishimoto (2010). For a range of mid-IR spectral indices between approximately  $\alpha_{\text{MIR}} = -0.6$  and  $\alpha_{\text{MIR}} = -2.5$  their models predict silicate features in emission or relatively shallow with values of the silicate strength approximately  $S_{\text{Si}} = -1$  to  $S_{\text{Si}} = 0.5$ . This behaviour implies that the observed nuclear mid-IR spectra of most of the (U)LIRG nuclei in our sample cannot be reproduced simply with clumpy torus models. It has been showed that they require foreground dust screen or a deeply embedded source (Levenson et al. 2007; Alonso-Herrero et al. 2013; Mori et al. 2014; Martínez-Paredes et al. 2015). The mid-IR spectrum of two (U)LIRG nuclei (IRAS 13197–1627 and IRAS 13349+2438) would be in principle reproduced by clumpy torus models as they show a relatively featureless continuum with no deep silicate feature.

In Fig. 7 (right panel) we note that the PG quasars and the RGs occupy a narrow stripe around  $S_{Si} \sim 0$  with  $\alpha_{MIR}$  ranging between -0.5 and -3, and would be in principle well reproduced by clumpy torus models. However, for the RGs there might be a non negligible contribution from synchrotron emission to the mid-IR spectrum. For PG quasars it has been shown that the full mid-IR spectra with the silicate feature in emission cannot always be fully reproduced with the Nenkova et al. (2008) clumpy torus models alone and need extra components (see Mor et al. 2009, and Martínez-Paredes et al. 2016 in preparation). Mason et al. (2013) found a similar result for the LLAGN NGC 3998 and showed that an optically thin dust model reproduced better the overall infrared emission of this AGN while producing the silicate feature in emission.

The nuclear mid-IR spectral index and silicate features of most Seyfert nuclei also fall in the region covered by the Hönig & Kishimoto (2010) clumpy torus models. There is a tendency for the type 1s to have on average flatter  $\alpha_{MIR}$  than type 2s, as already shown by Hönig et al. (2010). On the other hand, the Seyfert nuclei showing deeper silicate feature than predicted by the models are type 2s and suggest the presence of extended dust components not related to the torus (see also Alonso-Herrero et al. 2011; González-Martín et al. 2013). Although this subset of clumpy torus models plotted in this figure does not produce spectral indices as steep as  $\alpha_{MIR} = -3$ , it is likely due to the reduced parameter space (e.g., fixed angular width of the torus, optical depth of the clouds, and range of viewing angles) plotted in their figure. Indeed, figure 8 of Hönig & Kishimoto (2010) shows that steep mid-IR indices can be produced for instance for viewing angles  $i = 90$  deg (equatorial view). Also, the steep mid-IR continuum of NGC 2992 ( $\alpha_{MIR} = -2.8$ ) is reproduced by the Nenkova et al. (2008) clumpy torus models (García-Bernete et al. 2015). In a series of future papers we will present detailed comparisons between the observed spectra of Seyfert nuclei and PG quasars and predictions from clumpy torus models.

The silicate features seen in emission are rather muted and appear to peak at wavelengths longer than  $10 \mu\text{m}$ , as found in Spitzer/IRS spectra of type 1 Seyferts and QSOs (Hao et al. 2005). The spectra shown here have similar profiles, which may arise through optical depth effects in radiative transfer (Nikutta et al. 2009) or increased mean silicate grain sizes or from additional contributions from crystalline silicates such as enstatites which peak at longer wavelengths than the amorphous silicates typically seen in the ISM. Spoon et al. (2006) have argued that many ULIRGs contain significant levels of crystalline silicates in their absorption spectra and Kemper et al. (2011) suggest that the crystalline grains may be produced in the circumnuclear environment of the AGN.

### 4.3 Emission from the $11.3 \mu\text{m}$ PAH feature

The presence of PAH features in the nuclear regions of AGN can be used to trace the nuclear star formation activity. In particular PAH emission appears to be well suited to probe recent star formation as they trace the emission of both B stars and O stars (Peeters et al. 2004; Díaz-Santos et al. 2010). Although many AGN show  $11.3 \mu\text{m}$  PAH emission in their mid-IR spectra, these features appear weaker than

those observed in star-forming galaxies (Roche et al. 1991). However, Esquej et al. (2014) did not find evidence of strong suppression of the  $11.3 \mu\text{m}$  PAH emission in the nuclear regions of Seyferts in the Revised Shapley-Ames (RSA) catalog. The low EWs of the  $11.3 \mu\text{m}$  PAH feature in AGN have been interpreted as due to dilution by the presence of a strong AGN continuum rather than PAH destruction (Alonso-Herrero et al. 2014; Ramos Almeida et al. 2014b).

Seven Seyferts (Mrk 1066, NGC 2273, NGC 3227, NGC 4051, NGC 4253, NGC 5793, and NGC 7465) in the ESO/GTC sample show clear  $11.3 \mu\text{m}$  PAH emission in their nuclear spectra (see Fig. 5), although as found in other Seyfert nuclei the EW of the feature is lower than in star forming galaxies (González-Martín et al. 2013; Esquej et al. 2014; Alonso-Herrero et al. 2014). The nearly 50% detection rate for the Seyferts in our sample is similar to that of Seyferts in the RSA sample (Esquej et al. 2014). This again suggests that at least the carriers of the  $11.3 \mu\text{m}$  PAH feature do not get completely destroyed in the vicinity of Seyfert-like AGN at typical distances from the AGN of 45 pc in our sample and as close as 10 pc, as shown by Esquej et al. (2014).

Two of the LLAGN in our sample (NGC 4569 and NGC 4419) show bright nuclear PAH emission, whereas the other two (NGC 4579 and NGC 4258) do not and present the silicate feature in emission. At least for NGC 4569 the detection of bright  $11.3 \mu\text{m}$  PAH emission might be associated with the presence of massive young stars in the nuclear region (Maoz et al. 1998). Although this is a small sample of LLAGN, this variety of nuclear mid-IR spectral shapes agrees with the findings of Mason et al. (2012) from sub-arcsecond resolution mid-IR imaging data. They concluded that the nuclear mid-IR emission of LLAGN can be produced by several mechanisms (dust heated by AGN, dust heated by star formation, synchrotron emission) and might depend on the Eddington ratio of the AGN and the radio loudness. In any case, for the two LLAGN with PAH emission we can conclude that they have undergone star formation activity in the recent past and that the molecules responsible for the PAH features can survive at distances as close to the nucleus as 20 pc. The latter is well understood in the context of the survival of the PAH molecules at lower AGN luminosities even if they are closer to the AGN (see details in Esquej et al. 2014; Alonso-Herrero et al. 2014).

The nuclei of several (U)LIRGs in our sample: UGC 5101 (Martínez-Paredes et al. 2015), NGC 6240 South, Mrk 1073, IRAS 17208–0014 (Alonso-Herrero et al. 2014), and NGC 1614 (Pereira-Santaella et al. 2015) show clear nuclear  $11.3 \mu\text{m}$  PAH emission, whereas Mrk 463 East has a tentative detection. This means that in these (U)LIRGs the AGN does not completely dominate the nuclear (typical physical scales between 50 and 800 pc) mid-IR emission (see also e.g. Soifer et al. 2002; Mori et al. 2014; Alonso-Herrero et al. 2014; Martínez-Paredes et al. 2015). This is in contrast with the nuclei of the PG quasars and RGs, which have similar  $12 \mu\text{m}$  nuclear luminosities (see Fig. 6), but no bright nuclear PAH emission, at least in terms of the EW of the feature.

As can be seen from Table 5, the EW of the  $11.3 \mu\text{m}$  PAH feature of the AGN in our sample tend to be smaller than those measured from *Spitzer*/IRS spectra (see Hernández-Caballero & Hatziminaoglou 2011) for the same type of ob-

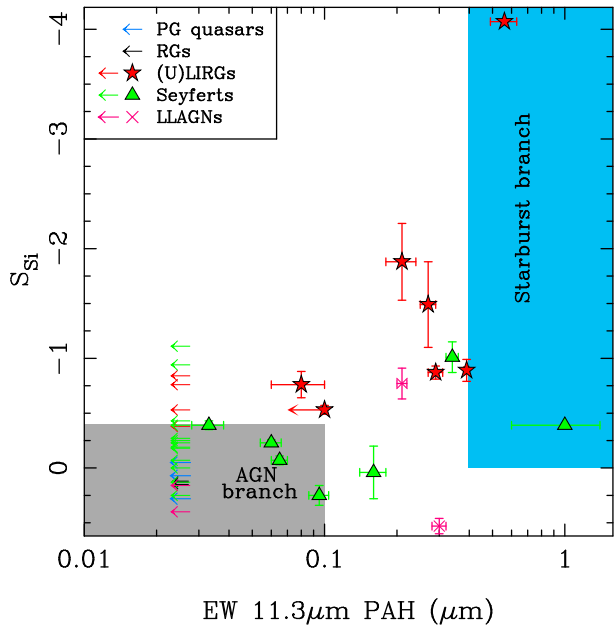


**Figure 8.** Nuclear EW of the  $11.3\mu\text{m}$  PAH feature against the strength of the silicate feature for the ESO/GTC large program AGN. For those AGN without a clear detection of the  $11.3\mu\text{m}$  PAH feature, the EW is plotted as an upper limit at the level of  $\sim 0.03\mu\text{m}$ . We plot the approximate location of the AGN and the starburst branches based on Hernan-Caballero & Hatziminaoglou (2011).

ject. This is well known (see figure 11 of Alonso-Herrero et al. 2014) and is understood in terms of an increased AGN contribution relative to that of star formation within the CanariCam (and other mid-IR instruments on 8-10 m-class telescopes) slit when compared to the almost 10 times wider IRS slit. It is only when there is a strong nuclear and highly concentrated starburst that the EW of the  $11.3\mu\text{m}$  PAH measured from CanariCam spectra would be similar to that of the IRS spectra.

In Fig. 8 we compare the EW of the  $11.3\mu\text{m}$  PAH feature with the strength of the silicate feature for the nuclear emission of our sample of AGN. These diagrams have been used in the literature to distinguish between AGN-dominated and starburst-dominated sources. As discussed by Hernan-Caballero & Hatziminaoglou (2011), using the  $11.3\mu\text{m}$  PAH feature instead of the  $6.2\mu\text{m}$  PAH feature has a number of advantages. First it avoids the water ice absorption feature in the wings of the  $6.2\mu\text{m}$  PAH feature in deeply obscured sources. Second, the spectral range required is narrower and in our case is accessible with ground-based telescopes for nearby AGN. In this diagram, the *Spitzer*/IRS starburst branch is nearly vertical with values of the EW typically between  $0.4$  and  $1\mu\text{m}$ . The AGN-dominated sources lie in a horizontal branch with EW typically of less than  $0.1\mu\text{m}$ , and the silicate feature in slight emission or absorption.

The nuclear mid-IR emission of PG quasars, RG and most of the Seyfert nuclei in our sample appears to be dominated by AGN emission, based on Fig. 8. On the physical scales probed by the CanariCam spectra only the nuclear mid-IR emission of the Seyfert NGC 5793 and the ULIRG IRAS 17208–0014 would appear to be dominated by star

formation. Most of the (U)LIRG nuclei in our sample (see also Soifer et al. 2002) and a few Seyfert nuclei appear to be composite sources, that is, these sources are examples with different degrees of contribution from the AGN and nuclear star formation to the observed nuclear emission.

#### 4.4 Fine structure lines

The most conspicuous mid-IR fine structure lines that can be observed from the ground are  $[\text{Ne II}]$  at  $12.81\mu\text{m}$  and  $[\text{S IV}]$  at  $10.51\mu\text{m}$ . The  $[\text{Ne II}]12.81\mu\text{m}$  line has a relatively low excitation potential and is mostly related to star formation activity in AGN (see e.g. Roche et al. 1991; Pereira-Santaella et al. 2010). Unfortunately,  $[\text{Ne II}]12.81\mu\text{m}$  falls very close to the edge of the CanariCam spectra and it is only seen or partly seen in some of the nearest galaxies in our sample (e.g., NGC 2273, NGC 2992, NGC 4419, NGC 4569, see Fig. 5).

The  $[\text{S IV}]10.51\mu\text{m}$  fine structure line has an intermediate excitation potential and therefore it has been observed both in AGN and star forming galaxies. Dasyra et al. (2011) detected this line in half of a large sample of AGN using *Spitzer*/IRS spectra and showed that it is a good tracer of the narrow line region emission in AGN. However, this line has also been observed in H II regions, for instance in M101 (Gordon et al. 2008) and star forming regions in local LIRGs (Pereira-Santaella et al. 2010).

As can be seen from Fig. 5, in general the  $[\text{S IV}]10.51\mu\text{m}$  line is not bright in the AGN in our sample and is only clearly detected in approximately one-third of them. These are mostly Seyfert nuclei both type 1 and 2 (for detections of this line at sub-arcsecond resolution see also Honig et al. 2008; Diaz-Santos et al. 2010; Gonzalez-Martın et al. 2013) and also in some (U)LIRG nuclei such as IRAS 13197–1627, NGC 1614 and Mrk 463 East and the PG quasar Mrk 841. Being a faint line with the added complication that it is inside the  $9.7\mu\text{m}$  broad silicate, it is likely that the non-detection in some CanariCam spectra is due to the limited signal-to-noise ratios in that part of the spectra.

## 5 SUMMARY

We have presented mid-IR Si-2 ( $\lambda_c = 8.7\mu\text{m}$ ) imaging and  $7.5 - 13\mu\text{m}$  spectroscopy ( $R = \lambda/\Delta\lambda \sim 175$ ) of a sample of 45 local AGN obtained with GTC/CanariCam through an ESO/GTC large program (ID 182.B-2005, PI Alonso-Herrero). The sample includes 4 LLAGN and 16 Seyfert nuclei at a median distance of 35 Mpc. It also contains 5 RG, 11 (U)LIRGs, and 9 PG quasars at a median distance of 254 Mpc. The ESO/GTC large program observations together with CanariCam GT observations are part of a mid-IR survey of local AGN aimed at the study of the obscuring material around active nuclei. The ESO/GTC large program imaging and spectroscopic observations were obtained under sub-arcsecond resolution conditions with a median value of  $0.3\text{arcsec}$  (FWHM).

The goal of this work was to present a brief overview of the mid-IR spectroscopic properties of the nuclear regions of the AGN in the ESO/GTC sample. The nuclear  $12\mu\text{m}$  luminosities of these AGN cover more than four orders of magnitude  $\nu L_{12\mu\text{m}} \sim 3 \times 10^{41} - 10^{46} \text{erg s}^{-1}$ . We summarize our main results as follows,

(i) We demonstrated that in terms of the nuclear  $12\ \mu\text{m}$  luminosity the sample is representative of the local population of mid-IR emitting AGN, based on the comparison with the Asmus et al. (2014) imaging atlas. The  $12\ \mu\text{m}$  luminosities of LLAGN and Seyfert nuclei are similar to those of other mid-IR spectroscopic observations obtained on sub-arcsecond resolution. The RGs, PG quasars and (U)LIRG nuclei in our ESO/GTC large program expand the existing sub-arcsecond resolution spectroscopy to more luminous and distant AGN. The CanariCam  $0.52\ \text{arcsec}$ -width slit probes typical physical regions of  $93\ \text{pc}$  in the LLAGN and Seyferts, and  $640\ \text{pc}$  in the rest of the sample.

(ii) We measured mid-IR spectral indices for the Seyfert nuclei, RG, LLAGN, and PG quasars in the range  $\alpha_{\text{MIR}} = -0.2$  to  $\alpha_{\text{MIR}} = -3$ , which are similar to those of other Seyfert nuclei observed on sub-arcsecond resolution. Some (U)LIRG nuclei show flatter mid-IR indices, which are in part due to the presence of PAH emission and/or deep silicate absorption.

(iii) We found that on sub-arcsecond scales most PG quasars and RGs as well as three LLAGNs, and one ULIRG/Sy1 nuclei show the silicate feature in emission. The majority of Seyfert nuclei show the feature in moderate absorption or slight emission. Most of the nuclei in our sample with deep silicate features ( $S_{\text{Si}} < -1$ ) are local LIRG and ULIRG and suggests that their AGN are likely embedded and obscured by dust not directly associated with the AGN.

(iv) We used a simple diagram comparing the spectral index  $\alpha_{\text{MIR}}$  and the strength of the silicate feature  $S_{\text{Si}}$  to show that most PG quasars, RGs, LLAGN, and Seyfert nuclei lie in the region covered by the clumpy torus models of Hönic & Kishimoto (2010). However, some RGs and PG quasars might require extra components to explain their mid-IR emission.

(v) We detected clear  $11.3\ \mu\text{m}$  PAH emission in the nuclear regions of 40% of the AGN in our sample where the spectral range allowed a measurement, namely 7 Seyferts, 5 (U)LIRGs, and 2 LLAGN. Based on an EW( $11.3\ \mu\text{m}$  PAH) vs.  $S_{\text{Si}}$  diagram, the mid-IR emission of PG quasars, RG and half of the Seyfert nuclei in our sample appears to be dominated by AGN emission, whereas only one ULIRG and one Seyfert nucleus would be mostly powered by star formation. Most (U)LIRG nuclei and a few Seyfert nuclei in our sample appear to be composite sources.

## ACKNOWLEDGMENTS

We thank an anonymous referee for suggestions that helped improve the paper. We are extremely grateful to the GTC staff for their constant and enthusiastic support to obtain the ESO/GTC large program observations presented in this paper. We thank Rhys Poulton for help with some of the spectroscopic analysis presented in this paper.

A.A.-H. acknowledges financial support from the Spanish Ministry of Economy and Competitiveness (MINECO) under the 2011 Severo Ochoa Program MINECO SEV-2011-0187. A.A.-H. and A.H.-C. acknowledge financial support from the Spanish Ministry of Economy and Competitiveness through grant AYA2012-31447, which is partly funded by the FEDER program, P.E. from grant AYA2012-31277, and L.C. from grant AYA2012-32295. C.R.A. acknowledges

financial support from the Marie Curie Intra European Fellowship within the 7th European Community Framework Programme (PIEF-GA-2012-327934). N.A.L. and R.E.M. are supported by the Gemini Observatory, which is operated by the Association of Universities for Research in Astronomy, Inc., on behalf of the international Gemini partnership of Argentina, Australia, Brazil, Canada, Chile, and the United States of America. C.P. acknowledges support from UTSA to help enable this research.

Based on observations made with the GTC, installed in the Spanish Observatorio del Roque de los Muchachos of the Instituto de Astrofísica de Canarias, in the island of La Palma. This research has made use of the NASA/IPAC Extragalactic Database (NED) which is operated by JPL, Caltech, under contract with the National Aeronautics and Space Administration.

## REFERENCES

- Alonso-Herrero A. et al. 2011, ApJ, 736, 82  
 Alonso-Herrero A., Pereira-Santaella M., Rieke G. H., Rigopoulou D. 2012, ApJ, 744, 2  
 Alonso-Herrero A. et al., 2013, ApJ, 779, L14  
 Alonso-Herrero A. et al. 2014, MNRAS, 443, 2766  
 Antonucci R. 1993, ARA&A, 31, 473  
 Asmus D., Gandhi P., Smette A., Hönic S. F., Duschl W. J., 2011, A&A, 536, A36  
 Asmus D., Hönic S. F., Gandhi P., Smette A., Duschl W. J., 2014, MNRAS, 439, 1648  
 Binggeli B., Sandage A., Tammann G. A. 1985, AJ, 90, 1681  
 Buchanan C. L., Gallimore J. F., O’Dea C. P., et al. 2006, AJ, 132, 401  
 Burtscher L. et al. 2015, A&A, 578, 47  
 Dasyra K. M. et al. 2011, ApJ, 740, 94  
 Diamond-Stanic A. M., Rieke G. H. 2012, ApJ, 746, 168  
 Díaz-Santos T., Alonso-Herrero A., Colina L., Packham C., Radomski J. T., Telesco C. M., 2008, ApJ, 685, 211  
 Díaz-Santos T., Alonso-Herrero A., Colina L., Packham C., Levenson N. A., Pereira-Santaella M., Roche P. F., Telesco C., 2010, ApJ, 711, 328  
 Elitzur M., Shlosman I. 2006, ApJ, 648, L101  
 Esquej P., Alonso-Herrero A., González-Martín O., Hönic S., Hernán-Caballero A., et al., 2014, ApJ, 780, 86  
 Feltre A., Hatziminaoglou E., Fritz J., Franceschini A., 2012, MNRAS, 426, 120  
 Gandhi P., Horst H., Smette A., Hönic S., Comastri A., Gilli R., Vignali C., Duschl W. 2009, A&A, 502, 457  
 García-Bernete I. et al. 2015, MNRAS, 449, 1309  
 García-Marín M., Colina L., Arribas S., Monreal-Ibero A. 2009, A&A, 505, 1319  
 Genzel R. et al., 1998, ApJ, 498, 579  
 Golombek D., Miley G. K., Neugebauer G. 1988, AJ, 95, 26  
 González-Martín O., Rodríguez Espinosa J. M., Díaz-Santos T., et al., 2013, A&A, 553, A35  
 González-Martín O., et al., 2015, A&A, 578, A74  
 Gordon K. D., Engelbracht C. W., Rieke G. H., Misselt K. A., Smith J.-D. T., Kennicutt R. C., Jr. 2008, ApJ, 682, 336  
 Goulding A. D., Alexander D. M., Bauer F. E., Forman

- W. R., Hickox R. C., Jones C., Mullaney J. R., Trichas M. 2012, *ApJ*, 755, 5
- Gorjian V., Werner M. W., Jarrett T. H., Cole D. M., Ressler M. E. 2004, *ApJ*, 605, 156
- Goulding A. D., Alexander D. M., 2009, *MNRAS*, 398, 1165
- Hao L. et al. 2005, *ApJ*, 625, L75
- Hatziminaoglou E., Hernán-Caballero A., Feltre A., Piñol Ferrer N. 2015, *ApJ*, 803, 110
- Hernán-Caballero A., Hatziminaoglou E. 2011, *MNRAS*, 414, 500
- Hönig S. F. et al. 2008, *A&A*, 485, L21
- Hönig S., Kishimoto M., 2010, *A&A*, 523, A27
- Hönig S. F., et al., 2010, *A&A*, 515, 23
- Horst H., Gandhi P., Smette A., Duschl W. J. 2008, *A&A*, 479, 389
- Ichikawa K., Packham C., et al. 2015, *ApJ*, 803, 57
- Imanishi M. 2009, *ApJ*, 694, 751
- Kemper F., Markwick A. J., Woods P. M. 2011, *MNRAS*, 413, 1192
- Laurent O., Mirabel I. F., Charmandaris V., Gallais P., Madden S. C., Sauvage M., Vigroux L., Cesarsky C. 2000, *A&A*, 359, 887
- Levenson N. A., Sirocky M. M., Hao L., Spoon H. W. W., Marshall J. A., Elitzur M., Houck J. R. 2007, *ApJ*, 654, L45
- Levenson N. A., Radoski J. T., Packham C., Mason R. E., Schaefer J. J., Telesco C. M. 2009, *ApJ*, 703, 390
- Lira P., Gonzalez-Corvalan V., Ward M., Hoyer S. 2008, *MNRAS*, 384, 316
- López-Rodríguez E., et al. 2014, *ApJ*, 793, 81
- López-Rodríguez E., et al. 2015, *MNRAS*, submitted
- Maoz D., Koratkar A., Shields J. C., Ho L. C., Filippenko A. V., Sternberg A. 1998, *AJ*, 116, 55
- Martínez Paredes M., Alonso-Herrero A., Aretxaga I. et al. 2015, *MNRAS*, in press (arXiv:1509.04396)
- Mason R. E., Geballe T. R., Packham C., Levenson N. A., Elitzur M., Fisher R. S., Perlman E. 2006, *ApJ*, 640, 612
- Mason R. E., Levenson N. A., Shi Y., Packham C., Gorjian V., Cleary K., Rhee J., Werner M. 2009, *ApJ*, 693, L136
- Mason R. E., Lopez-Rodriguez, E., Packham C., Alonso-Herrero A., Levenson N. A., Radoski J., Ramos Almeida, C., Colina L., Elitzur M., Aretxaga I., Roche P. F., Oi N. 2012, *AJ*, 144, 11
- Mason R. E., Ramos Almeida, C., Levenson N. A., Nemmen R., Alonso-Herrero A. 2013, *ApJ*, 777, 164
- Mor R., Netzer H., Elitzur M. 2009, *ApJ*, 705, 298
- Mori T. I. et al. 2014, *PASJ*, 66, 93
- Moshir M. et al., 1990, *IRAS Faint Source Catalogue*, version 2.0
- Nenkova M., Sirocky M. M., Nikutta R., Ivezić Z., Elitzur M., 2008, *ApJ*, 685, 160
- Netzer H. 2015, *ARA&A*, 53, 365
- Nikutta R., Elitzur M., Lacy M. 2009, *ApJ*, 707, 1550
- Packham P., Telesco C. M., Hough J. H., Ftaclas C. 2005, *Rev. Mex. de Astron. Astrof. Conference Series*, 24, 7
- Peeters E., Spoon H. W. W., Tielens A. G. G. M., 2004, *ApJ*, 613, 986
- Pereira-Santaella M., Diamond-Stanic A. M., Alonso-Herrero A., Rieke G. H. 2010, *ApJ*, 725, 2270
- Pereira-Santaella M., Alonso-Herrero A., et al. 2010, *ApJS*, 188, 447
- Pereira-Santaella M., Colina L., Alonso-Herrero A. et al. 2015, *MNRAS*, in press (arXiv:1509.07765)
- Ramos Almeida C., Levenson N. A., Alonso-Herrero A. et al. 2011, *ApJ*, 731, 92
- Ramos Almeida C., Alonso-Herrero A., Levenson N. A., Asensio Ramos A., Rodríguez Espinosa J. M., González-Martín O., Packham, C., Martínez M. 2014a, *MNRAS*, 439, 348
- Ramos Almeida C. et al. 2014b, *MNRAS*, 445, 1130
- Reach W. T. et al. 2005, *PASP*, 117, 978
- Rice W., Lonsdale C. J., Soifer B. T., Neugebauer G., Kopan E. L. Lloyd L. A., de Jong T., Habing H. J. 1988, *ApJS*, 68, 91
- Roche P. F., Aitken D. K., Smith C. H., Ward M. J., 1991, *MNRAS*, 248, 606
- Roche P. F., et al., 2006, *MNRAS*, 367, 1689
- Roche P. F., Packham C., Aitken D. K., Mason R. E. 2007, *MNRAS*, 375, 99
- Roche P. F., Alonso-Herrero A., González-Martín O. 2015, *MNRAS*, 449, 2598
- Ruschel-Dutra D., Pastoriza M., Riffel R., Sales D. A., Winge C. 2014, *MNRAS*, 438,3434
- Sako S. et al. 2003, *PASP*, 115, 1407
- Sales D. A., Pastoriza M. G., Riffel R., Winge C., 2013, *MNRAS*, 429, 2634
- Sanders D. B., Mazzarella J. M., Kim D.-C., Surace J. A., Soifer B. T., 2003, *AJ*, 126, 1607
- Schmidt M., & Green R. F. 1983, *ApJ*, 269, 352
- Shi Y., Rieke G. H., Hines D. C. et al. 2006, *ApJ*, 653, 127
- Shi Y., Ogle P., Rieke G. H., et al. 2007, *ApJ*, 669, 841
- Smith J. D. et al., 2007, *ApJ*, 656, 770
- Snijders L., van der Werf P. P., Brandl B. R., Mengel S., Schaerer D., Wang Z. 2006, *ApJ*, 648, L25
- Soifer B. T., Neugebauer G., Matthews K. et al. 2000, *AJ*, 119, 509
- Soifer B. T., Neugebauer G., Matthews K., Egami E., Weinberger A. J. 2002, *AJ*, 124, 2980
- Spoon H. W. W. et al. 2006, *ApJ*, 638, 759
- Spoon H. W. W. et al. 2007, *ApJ*, 654, L49
- Sturm E. et al. 2005, *ApJ*, 629, L21
- Telesco C. M., Ciardi D., French J., et al., 2003, in *SPIE Conference Series*, Vol. 4841, 913
- Thompson G. D., Levenson N. A., Uddin S. A., Sirocky M. M. 2009, *ApJ*, 697, 182
- Tommasin S., Spinoglio L., Malkan M. A., Smith H., González-Alfonso E., Charmandaris V. 2008, *ApJ*, 676, 836
- Tommasin S., Spinoglio L., Malkan M. A., Fazio G. 2010, *ApJ*, 709, 1257
- Wu Y., Charmandaris V., Huang J., Spinoglio L., Tommasin S. 2009, *ApJ*, 701, 658
- Yan H., Wang J.X., Liu T. 2015, *ApJ*, 799, 91
- Yuan T.-T., Kewley L. J., Sanders D. B. 2010, *ApJ*, 709, 884